

Geochemistry, Geophysics, Geosystems®



RESEARCH ARTICLE

10.1029/2023GC011196

Special Section:

Through the Arctic Lens:
Progress in Understanding the
Arctic Ocean, Margins and
Landmasses

Key Points:

- New volcanic rock samples are dredged from Vesteris Seamount in the SW Greenland Sea
- Sample analysis shows geochemical evidence of deep mantle component and continental crust remobilization
- Melting underneath Vesteris was enhanced by steep lithospheric thickness change that allowed channeling of the Iceland plume branch

Supporting Information:

Supporting Information may be found in the online version of this article.

Correspondence to:

L. Beloša,
lea.belosa@geo.uio.no

Citation:

Beloša, L., Callegaro, S., Meyzen, C. M., Gaina, C., Polteau, S., Bizimis, M., & Mazzini, A. (2024). Deep mantle component and continental crust remobilization in the source of Vesteris Seamount, East Greenland margin. *Geochemistry, Geophysics, Geosystems*, 25, e2023GC011196. <https://doi.org/10.1029/2023GC011196>

Received 21 AUG 2023






Accepted 9 DEC 2023

Author Contributions:

Conceptualization: L. Beloša, S. Callegaro

Data curation: L. Beloša, S. Polteau, M. Bizimis, A. Mazzini

Deep Mantle Component and Continental Crust Remobilization in the Source of Vesteris Seamount, East Greenland Margin

L. Beloša¹ , S. Callegaro¹ , C. M. Meyzen², C. Gaina¹ , S. Polteau³, M. Bizimis⁴ , and A. Mazzini^{3,5} 

¹Centre for Planetary Habitability, University of Oslo, Oslo, Norway, ²Department of Geosciences, University of Padova, Padova, Italy, ³Institute for Energy Technology, Kjeller, Norway, ⁴School of Earth, Ocean and Environment, University of South Carolina, Columbia, SC, USA, ⁵Department of Geosciences, University of Oslo, Oslo, Norway

Abstract Vesteris Seamount is a large Quaternary intraplate submarine volcano in the SW Greenland Sea, about 1,000 km NE of Iceland and 300 km NW of the Mohn's spreading ridge, whose mode of formation remains unsolved. We present geochemical data for new samples dredged from the Vesteris edifice, including major, trace elements and Sr-Nd-Pb-Hf isotopes. The isotopic characteristics of the alkaline lavas, covering the basanite/tephrite to benmoreite range, indicate the involvement of depleted and enriched mantle components. The source is dominated by the depleted mantle (85%–90%) and a deep enriched component possibly supplied by the Iceland Plume (IP) (10%–15%). Additional source enrichment was due to recycled crust and sub-continental lithospheric mantle, as suggested by Hf isotopes (0.283147 ± 0.000005) measured for the first time in Vesteris lavas and by a decoupling in Pb isotopes evidenced by relatively low-radiogenic ²⁰⁷Pb/²⁰⁴Pb (15.510) and high-radiogenic ²⁰⁸Pb/²⁰⁴Pb (38.554) with respect to the Northern Hemisphere Reference Line. We interpret the geochemical results using existing knowledge about the regional lithospheric and upper mantle structure. Our findings suggest that a deep (ca. 420–320 km) mantle anomaly, with seismological characteristics of the Iceland mantle plume, extends from East Greenland to the north of Jan Mayen Fracture Zone. The regional lithospheric thinning toward the Greenland Basin enabled the melting events that produced the Vesteris seamount. This lateral NNE-directed flow lobe of the Iceland plume may have carved and transferred enriched components from the continental lithospheric margin of Greenland north of Scoresby Sund toward the Vesteris source.

Plain Language Summary This study investigates the formation of Vesteris Seamount, the largest submarine volcano in the Greenland Sea, situated north of Iceland and the Jan Mayen Fracture Zone and east of the Greenland continental margin. Given the isolated position of Vesteris, it is challenging to define its formation mechanisms and the mantle source. This study presents geochemical data by analyzing samples dredged from Vesteris' flanks. A deep mantle component, similar to the Iceland plume, seems to contribute to the mantle source of Vesteris magmas and the regional depleted asthenosphere. However, our results also suggest a contribution of an enriched component. This could be the sub-continental mantle lithosphere (SCLM) and a crustal component. These components could have been transported from the Northeastern Greenland Margin, North of Scoresby Sund, along with the mantle flow. Subsurface seismic tomography images indicate an NNE-directed flow lobe from the mantle plume under Iceland. We suggest that this setting played an important role in the seamount formation and explain the isotope signatures of SCLM-like and crustal components by deep mantle carving of the western Greenland margin.

1. Introduction

Volcanic seamounts are dynamic features across oceanic basins and form in diverse tectonic settings. While most are located near mid-ocean ridges (MOR) and trenches linked to seafloor spreading and subduction-related volcanism, respectively (White, 2005), others occur away from active plate boundaries in intra-plate tectonic settings. Mantle plume interactions with lithosphere can explain some intraplate volcanism, particularly leading to the age-progressive linear seamount chains (e.g., the Hawaiian-Emperor seamount chain) (Morgan, 1972; Wilson, 1963). In contrast, the origin of solitary intraplate seamounts, often less conspicuous and found sporadically on the seafloor, remains enigmatic (e.g., Batiza, 1982; Gaina, Blischke, et al., 2017). Isolated seamounts

© 2024 The Authors. *Geochemistry, Geophysics, Geosystems* published by Wiley Periodicals LLC on behalf of American Geophysical Union.

This is an open access article under the terms of the [Creative Commons Attribution License](https://creativecommons.org/licenses/by/4.0/), which permits use, distribution and reproduction in any medium, provided the original work is properly cited.

Formal analysis: M. Bizimis
Funding acquisition: C. Gaina, S. Polteau, A. Mazzini
Investigation: L. Beloša
Methodology: L. Beloša, S. Polteau, M. Bizimis
Project Administration: C. Gaina, A. Mazzini
Resources: S. Callegaro, C. M. Meyzen, S. Polteau
Software: L. Beloša, C. Gaina
Supervision: S. Callegaro, C. Gaina, A. Mazzini
Validation: S. Callegaro, C. M. Meyzen, C. Gaina, S. Polteau, M. Bizimis, A. Mazzini
Visualization: L. Beloša, S. Callegaro, A. Mazzini
Writing – original draft: L. Beloša, S. Callegaro, C. M. Meyzen
Writing – review & editing: L. Beloša, S. Callegaro, C. M. Meyzen, C. Gaina, S. Polteau, M. Bizimis, A. Mazzini

can have a random spatial distribution and lower volcanic activity than seamount chains. Still, they can form long-lived volcanic centers rising a few kilometers above the seafloor (Wessel et al., 2010).

Volcanic seamounts are generated by igneous processes and exhibit strong axial symmetry. As they grow, the complex distribution of stresses that form rift zones and fissure eruptions cause the seamounts to lose their initial shape. Many seamounts exhibit structures from combining single magma feeder tubes and fissure linear eruption. Therefore, the morphology of volcanic seamounts is controlled by eruption rates, magma composition and viscosity, and pre-existing topography (e.g., Schmidt et al., 2000).

The composition of isolated seamounts often features alkalic volcanic rocks, such as basanite, nephelinite, or even phonolites. These lithologies generally indicate that the mantle source of magmas forming these seamounts undergoes partial melting to low degrees and great depths; therefore, it is distinct from the sources generating volcanic material at MORs or subducting zones. Various mechanisms have been proposed to elucidate the generation of intraplate seamounts, involving scenarios such as pressure release causing partial melts in the asthenosphere, small-scale sublithospheric convection, and shear-driven upwelling resulting from asthenospheric and sub-lithospheric heterogeneities or related to the proximity of mantle plumes (e.g., Ballmer et al., 2009; Buck & Parmentier, 1986; Conrad et al., 2010; Forsyth et al., 2006; Haxby & Weissel, 1986; Hirano et al., 2006; Sandwell & Fialko, 2004). The geochemistry and petrology of seamount rocks can unveil the processes involved in their formation.

In this study, we investigate the origin of the Vesteris Seamount, a large (33 × 27 km; Moreno et al., 2021) solitary volcanic construction located in the Greenland Sea, Northeast (NE) Atlantic, with a summit dated at 0.65–0.010 Ma, and a basement probably younger than 7–13 Ma (Mertz & Renne, 1995). This volcano is ca. 300 km away from the Greenland coast, 300 km from Mohn's Ridge, the closest active plate boundary, and 220 km north of the large and complex Jan Mayen Fracture Zone (K. M. Haase & Devey, 1994; Mertz & Renne, 1995; Moreno et al., 2021) (Figure 1).

Over the years, explanations for the formation of Vesteris swung between theories involving lithospheric extension and plume-driven processes. Based on seismic reflection data collected by the ARKTIS II/4 (1984) marine expedition, an initial suggestion indicated that the volcanic activity at Vesteris might be related to a crustal weakness zone (Hempel et al., 1991). A follow-up survey in 1990 (ARKTIS VII/1) led to the interpretation of Vesteris magmas as being produced by a region with low seismic velocity and transported through lithospheric fractures caused by the stress field exerted by the development of Mohn's and Kolbeinsey MOR (K. M. Haase & Devey, 1994). Regarding the geochemical composition of Vesteris rocks, Cherkis et al. (1994) highlighted that they are silica-undersaturated compared to the neighboring Jan Mayen Island. This discrepancy may indicate distinct melting regimes or mantle sources for the two volcanic bodies (Mertz & Renne, 1995). A mantle plume origin for Vesteris was discarded by Mertz and Renne (1995) due to the lack of an associated dome anomaly in the vicinity of Vesteris (K. M. Haase & Devey, 1994; Vogt et al., 1982). Zhang et al. (2020) recently rejuvenated the plume hypothesis by showing that the Vesteris Plateau (VP), an elevated region (~1,500 m) surrounding the Vesteris Seamount, lies above an anomalous broad low shear-wave seismic velocity anomaly (LVZ). The LVZ is most prominent at mantle depths of 420–320 km and extends up to 150–100 km depth (Auer et al., 2014; Marquart et al., 2007; Pilidou et al., 2005; Zhang et al., 2020). An excess crust volume of $\sim 2.33 \times 10^5 \text{ km}^3$ makes this plateau comparable with other North Atlantic elevated bathymetric structures like the Bermuda Rise east of North America (Wang et al., 2011). Such seismic anomaly could reflect the presence of a hot mantle below the VP, interpreted by Zhang et al. (2020) as the northernmost expression of the Iceland-Jan Mayen plume. A comprehensive study of the Vesteris Seamount area that revisits the connection between its geochemical signature and the surrounding lithospheric and mantle structure is presently lacking.

This study tests the hypothesis that deep mantle anomalies (possibly the Iceland plume [IP]) contributed to the formation of Vesteris Seamount. First, by analyzing a set of samples dredged from Vesteris flanks, we present whole-rock major and trace element and radiogenic isotope data (Sr-Nd-Pb and, for the first time for Vesteris, Hf isotopes). Next, we examine the available regional lithospheric thickness models and mantle seismic tomography to identify possible sources for this submarine volcanism. The presented geochemical results are integrated into a regional framework to contextualize the formation of Vesteris into the NE Atlantic geodynamic evolution.

2. Regional Geologic Context and Vesteris Edifice

Following the continental breakup between Eurasia and Greenland in the early Eocene (i.e., Talwani & Eldholm, 1977), the NE Atlantic and its northern sub-basins (i.e., Greenland, Lofoten, Norway Basin; Figure 1a)

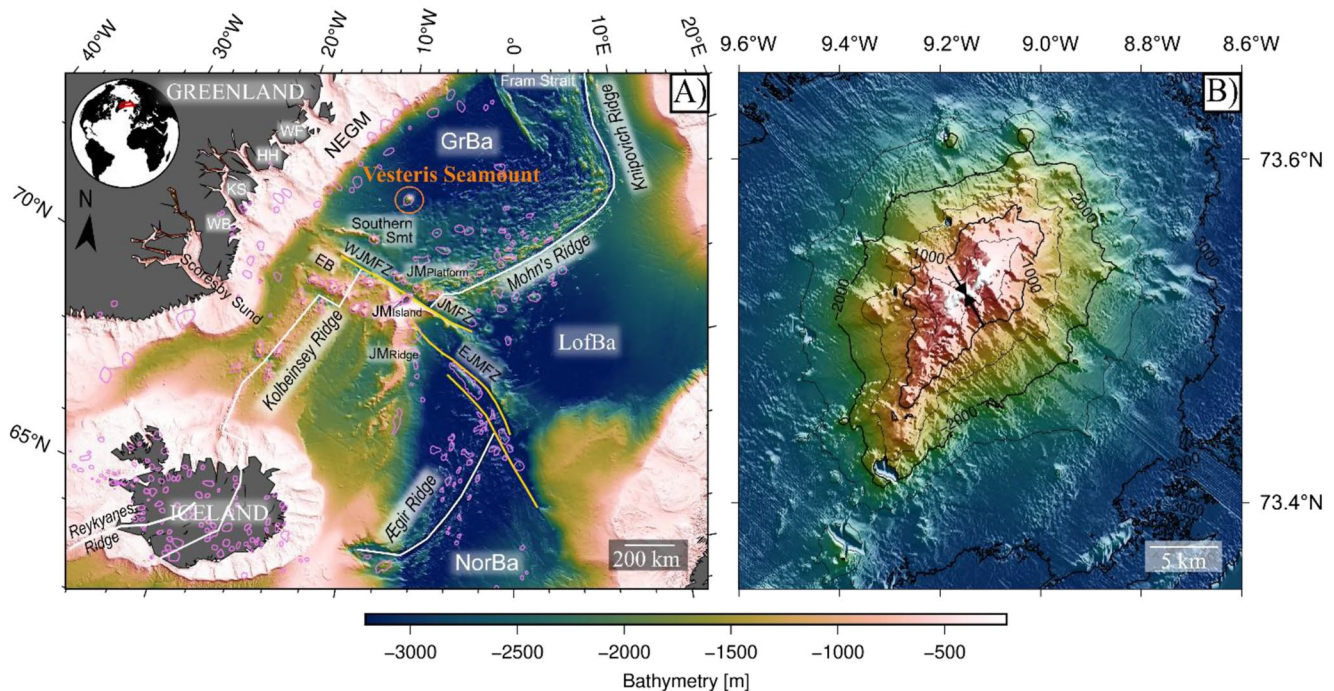


Figure 1. (a) NE Atlantic regional bathymetry (GEBCO, 2021). Mid-ocean ridge segments (active and extinct) are represented as white lines and fracture zones as yellow lines (Müller et al., 2016). Pink polygons indicate the location of volcanic edifices (Gaina, Blischke, et al., 2017). The orange circle marks the Vesteris Seamount's location. (b) Vesteris Seamount bathymetry (acquired by the MSM86 cruise (Moreno et al., 2021)). Dredged transects indicated by black arrows: EGS 12-93D (SOL—73.537701N; 9.183944W, EOL—73.520879N; 9.149131W) and EGS 12-94D (SOL—73.502981N; 9.113111W, EOL—73.521535N; 9.149729W). Abbreviations: EB, Eggvin Bank; EJMfZ, East Jan Mayen Fracture Zone; GrBa, Greenland Basin; HH, Hold with Hope; JMI, Jan Mayen Island; JMR, Jan Mayen Ridge; JMP, Jan Mayen Platform; KS, Kap Simpson; LofBa, Lofoten Basin; NEGM, Northeast Greenland Margin; NorBa, Norway Basin; WB, Werner Bjerger; WF, Wollaston Forland; WJMfZ, Western Jan Mayen Fracture Zone.

formed between the two continents. The accompanying large-scale magmatism that occurred before, during, and after the breakup was closely connected to the impingement of a mantle plume below Greenland (i.e., Vogt et al., 1982). The interaction between the mantle plume (presently active under Iceland) and the NE Atlantic lithosphere led to a large igneous province formation (the North Atlantic Igneous Province, NAIP; 62–56 Ma, i.e., Saunders et al., 1997). Later on, this was followed by a shift in plate boundary north of Iceland from the Ægir to the Kolbeinsey MOR completed in the Late Oligocene (26 Ma, Chron C7; Gernigon et al., 2012). Currently, the slow-spreading active MOR is split into several segments that run through the NE Atlantic Ocean, intersecting Iceland, where the mantle plume built the island and continues to generate large amounts of magma. The ridge is offset to the east by the Jan Mayen Fracture Zone and continues northwards to the Arctic Ocean via the narrow Fram Strait (Figure 1a).

The NE Atlantic seafloor is littered with seamounts (Figure 1). Gaina, Blischke, et al. (2017) defined 175 features with elevations greater than 500 m and 12 features taller than 1,000 m. The distribution of seamounts on the smooth and older oceanic crust (54–50 Ma) is related to a spreading rate increase and higher magmatic productivity. Late Eocene-Early Miocene seamount clusters are located on the rough oceanic crust in the Irminger, Iceland, and Norway basins. They are related to kinematic changes, MOR segment readjustments, and formation of a fracture zone in the southern part of NE Atlantic. Seamounts located on the Mid-Miocene to Present rough crust of Lofoten and Greenland basins and Kolbeinsey ridge flanks may also be associated with ridge propagation and V-shaped ridges. The distribution and origin of the NE seamounts are linked to variations in seafloor spreading rates, spatio-temporal IP activity, and main tectonic events affecting the region (i.e., Schilling & Noe-Nygaard, 1974; Kempton et al., 2000). Gaina, Blischke, et al. (2017) also pointed out the asymmetric distribution of the younger Mid-Miocene-Present seamounts in the conjugate Greenland and Lofoten basins in the Greenland Sea. They noted that spatial and temporal links between the IP and the Jan Mayen Fracture Zone may have played a role in producing submarine volcanism in the northern part of NE Atlantic. Most seamounts and submarine volcanic plateaus south and north of the Jan Mayen Fracture Zone are related to either MOR

formation, the activity of the Icelandic plume (O'Connor et al., 2000), or to another mantle anomaly interpreted in some studies as the Jan Mayen plume (Elkins et al., 2016; Kharin & Eroshenko, 2014; Schilling et al., 1999).

Among these structures, the Vesteris Seamount in the Greenland Basin (73° 30'N and 9° 10'W, Figure 1b) is the largest seamount on the NE Atlantic oceanic crust. Vesteris sits on ca. 50 km thick and 40.3–43.4 Ma old oceanic lithosphere (Gaina et al., 2009; Gaina, Blischke, et al., 2017; Steinberger & Becker, 2018; Zhang et al., 2020). This volcanic edifice, exceptional because of its dimensions and position, rises from a depth of ~3,225 m to reach 137 m below sea level with a total eruptive volume of ca. 800 km³ (Moreno et al., 2021), comparable to the large seamounts observed in the Pacific Ocean, where fast-spreading dominates (Vogt & Smoot, 1984). The edifice is quasi-conical with an elongated prolongation SE from the main edifice, interpreted as *en echelon* rift extrusion (K. M. Haase & Devey, 1994). Its orientation is sub-parallel to Mohn's and Kolbeinsey's active MOR, which prompted suggestions that these bathymetric features may be related (Grønlie et al., 1979; Hempel et al., 1991). A recent study based on detailed bathymetry data offers detailed observations about the seamount surface, as summarized below (Moreno et al., 2021). The summit has a smooth surface, low relief, and a slope angle of less than 10°. Apart from the main cone, Vesteris has several satellite volcanic cones at the NW and SE ends of the edifice and radial ridges. They strike perpendicularly to the summit and the main ridge, which may indicate the episodic building of the edifice. Several other morphological features with different slope and ruggedness indexes, described as a distribution of terrain heterogeneity, have been observed (Moreno et al., 2021). Smaller volcanic cones and hummocky lava flows at the basement exhibit slope angles up to 45°. Most cones crowning radially distributed irregular ridges are characterized by slopes above 20°. Irregular elongated ridges accommodate volcanic debris fans having steep slope angles as well. They represent a boundary between low-ruggedness volcanoclastic terrains (<20) with smooth surfaces and hummocky lava flows with high ruggedness (>20). Moreno et al. (2021) suggest the following model to explain the complex morphology of Vesteris seamount: (a) widespread effusive volcanism erupted from a central vent during the earliest stage and related to deep, regional extensional lithospheric stresses; (b) the intermediate stage saw frequent dike-fed eruptions, controlled by a local stress field within the edifice, and (c) during the latest stage of growth, toward shallower water depths, hydro-magmatic eruptions deposited easily erodible hyaloclastite at the summit, and the edifice suffered deconstruction by flank collapses and dislocation of cross-cutting ridges.

Note that this solitary volcano is much younger than its substrate, dated to 40.3–43.4 Ma, based on magnetic anomalies (C18–C20; Gaina et al., 2009, 2017b). Early ⁴⁰Ar/³⁹Ar studies pointed toward an episodic building of Vesteris, with trachybasaltic and tephritic eruptions between 0.50–0.65 Ma, followed by an eruptive phase of mugearitic composition around 0.010–0.085 Ma (Mertz & Renne, 1995).

3. Methods

3.1. Sampling Campaign and Selection

In 2012, Vesteris Seamount was sampled with two dredge profiles during a research campaign (East Greenland Sampling, EGS-2012) onboard RV Sermilik II. The dredge was a heavy-duty 80 × 40 cm steel frame with teeth on one side and a 1 m deep chain bag lined with a fisherman's net in nylon to retain smaller fragments. The samples were collected along opposite SE (EGS12-94D) and NW facing slopes (EGS12-93D, Figure 1b, Table S1) by lowering the dredge to ca. 900 m depth and dragging it on the flanks toward the summit at 165 and 186 m, respectively. The dredges recovered ca. 5 kg of angular to sub-rounded volcanic rock fragments (generally 3–5 cm diameter) coated with brown-reddish weathered surfaces (Figure S1 in Supporting Information S1). The dredge recovered abundant organic material (sponges, coral fragments). It did not contain any hemipelagic sediment along with the rock fragments. Most of the samples had sides with freshly broken surfaces, suggesting that they were ripped directly from steep escarpments (Moreno et al., 2021), while some samples were sub-rounded. Dredge might have crossed different terrains, U-shaped volcanoclastic terrains, and hummocky lava flows.

Sample selection was conducted to identify the representative, freshest, and largest lava fragments based on macroscopic petrographic observations. A total of 23 samples selected for chemical analyses were first carefully washed in purified water to remove potential surface contaminants. For whole-rock analyses, <1 cm thick slabs were cut from each sample, keeping only the fresh core. Slabs were subsequently crushed with a hammer, and individual fragments were hand-picked under a binocular microscope to avoid any weathered surfaces. Hand-picked samples were repeatedly washed in ultrasonic baths of purified water and ethanol for 60 min, repeatedly and then dried. The hand-picked fractions were powdered in an agate mortar and weighted.

3.2. Analyses

Whole-rock major elements were measured on a subset of six samples using an Inductively Coupled Plasma Optical Emission (ICP-OES), following the four Lithores-Research routine at Actlabs (Activation Laboratories Ltd., Canada), and another six samples at the Franklin and Marshall College (Lancaster, Pennsylvania) using Lithium Tetraborate fusion Malvern PANalytical, Inc. Zetium X-ray fluorescence (Boyd & Mertzman, 1987). Additional 11 samples were used to analyze TiO_2 , Al_2O_3 , Fe_2O_3 , MnO , MgO , and CaO , using Thermo ELEMENT 2 HR-Inductively Coupled Plasma Mass Spectrometry (ICP-MS) at the Center for Elemental Mass Spectrometry (CEMS), University of South Carolina (USC). Typical uncertainties are 2% for all major elements except MnO and P_2O_5 .

Whole-rock trace element analyses were performed on 16 samples using a Thermo ELEMENT 2 HR-ICP-MS at the CEMS, USC, and six following the four Lithores-Research routine at Actlabs (Activation Laboratories Ltd., Canada). Indium was the internal standard, standardized against the BHVO-2 USGS rock material using the preferred concentrations from the GEOROC database. The major cations (SiO_2 , MgO , Fe_2O_3 , Al_2O_3 , CaO , Na_2O , K_2O , P_2O_5 , TiO_2 , and MnO) and trace elements were analyzed using the Medium Resolution ($\Delta M = 3,000$) on the ELEMENT 2 HR-ICP-MS. Repeated analyses of unknown solutions reproduced to better than 3% (typically 1%). Therefore, the accuracy of the data is estimated by the BCR-2 (USGS) and JB-2 basalt (Geological Society of Japan) materials run as unknowns. Rare-Earth Element (REE) reproducibility was produced within 3%–4% for other elements.

Sr-Nd-Pb-Hf isotopic compositions were analyzed on 12 samples at the CEMS, USC, on a Neptune MC-ICP-MS. About 120 mg of powdered samples were leached and then analyzed following laboratory standard techniques (Béguelin et al., 2017; Frisby et al., 2016). Each digested sample was split to run different fractions for the different isotope systems, all from a single dissolution. Measured $^{87}\text{Sr}/^{86}\text{Sr}$ ratios were corrected for mass fractionation using $^{86}\text{Sr}/^{88}\text{Sr} = 0.1194$, and krypton interference on ^{86}Sr was corrected online using $^{83}\text{Kr}/^{86}\text{Kr} = 0.66474$. Accuracy was monitored every 2–3 samples by measuring the NIST SRM987 standard (Ehrlich et al., 2001), giving a mean of $^{87}\text{Sr}/^{86}\text{Sr} = 0.710307 \pm 0.000009$ (2 standard deviations, $n = 16$). All the $^{87}\text{Sr}/^{86}\text{Sr}$ data are reported relative to $^{87}\text{Sr}/^{86}\text{Sr} = 0.710248$. The mean $^{87}\text{Sr}/^{86}\text{Sr}$ value for the BCR-2 USGS standard obtained during the analyses is 0.705023 ± 0.000006 ($n = 4$), consistent with the recommended values (Weis et al., 2006). Sr procedural blanks were less than 50 pg. Measured $^{143}\text{Nd}/^{144}\text{Nd}$ isotope ratios were corrected for mass fractionation using $^{146}\text{Nd}/^{144}\text{Nd} = 0.7219$. The JNdi-1 reference material was determined at $^{143}\text{Nd}/^{144}\text{Nd} = 0.512090$ (± 0.000009 , $n = 10$), and the data is reported against the accepted value of 0.512115 for this material. The mean $^{143}\text{Nd}/^{144}\text{Nd}$ value for BCR-2 obtained during the analyses is 0.512638 ± 0.000011 ($n = 4$), identical to the recommended values published by Weis et al. (2006). Measured $^{176}\text{Hf}/^{177}\text{Hf}$ isotopes were corrected for mass fractionation using $^{179}\text{Hf}/^{177}\text{Hf} = 0.7325$. An in-house Hf solution was determined at $^{176}\text{Hf}/^{177}\text{Hf} = 0.282134 \pm 0.000004$ ($n = 11$), corresponding to the JMC 475 original solution of 0.282155; data is reported against the accepted value of 0.282160 for the JMC-475 material. $^{176}\text{Hf}/^{177}\text{Hf}$ for BCR-2 was determined at 0.282664 ± 0.000006 ($n = 4$), identical to the literature (Weis et al., 2007). Pb isotopes were corrected for mass fractionation using the Tl doping technique. NBS 981 was determined at $^{206}\text{Pb}/^{204}\text{Pb} = 16.9345 \pm 0.0008$, $^{207}\text{Pb}/^{204}\text{Pb} = 15.4873 \pm 0.0012$, $^{208}\text{Pb}/^{204}\text{Pb} = 36.6828 \pm 0.004$, and the data is reported against the SRM 981 triple spike values of Abouchami et al. (2000). BCR-2 was determined at $^{206}\text{Pb}/^{204}\text{Pb} = 18.762 \pm 0.0007$, $^{207}\text{Pb}/^{204}\text{Pb} = 15.6194 \pm 0.0009$, $^{208}\text{Pb}/^{204}\text{Pb} = 38.7367 \pm 0.0032$.

4. Results

Here, we report novel petrography and geochemistry data from a collection of rocks dredged from the Vesteris Seamount (Table S1). We analyzed the samples and performed the geochemical analyses to determine their composition and investigate their magmatic source. No geochemical data from this rock collection have ever been published before.

4.1. Petrography

Extrusive samples dredged from the Vesteris Seamount are generally dark gray to black with brown-reddish surfaces. The vesicularity of lavas ranges from 5% to 20% (Figures 2a and 2c). The vesicles are mostly void, only occasionally filled (amygdalae) with secondary calcite, zeolites, or Fe-Mn oxide-hydroxide crusts.

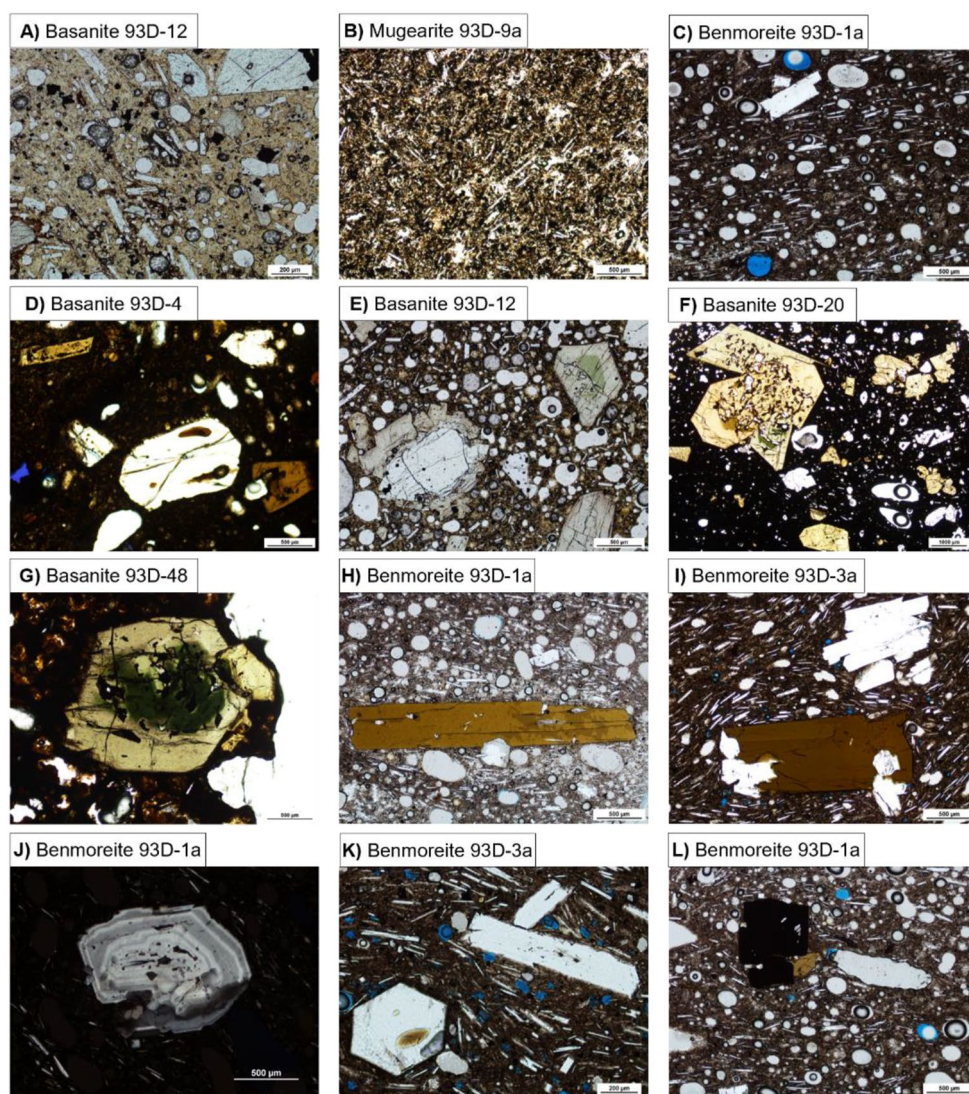


Figure 2. Micro-photographs of Vesteris Seamount samples. Groundmass of (a) basanite, (b) aphyric mugearite, (c) benmoreite; (d) subhedral olivine with melt inclusions, (e) left—olivine with a rim of clinopyroxene, right—zoned clinopyroxene with a green core, (f) clinopyroxene glomerocryst with a resorbed core, (g) zoned clinopyroxene with a green core, (h) euhedral amphibole with needle-like apatite inclusions, (i) top—plagioclase phenocrysts, bottom—glomerocrysts of plagioclases and amphibole, (j) oscillatory zoned plagioclase in polarized light, (k) top—plagioclase, bottom—euhedral h aüyne with melt inclusion, (l) glomerocryst of oxide with amphibole.

The samples were classified into five groups based on their distinctive mineral assemblages and whole-rock major element compositions (Table S1, Figure 3). The sample set consists of alkali basalt, basanites/tephrites, mugearites, phono-tephrites, and benmoreites. Most lavas are porphyritic, and phenocrysts are generally <1 mm in size (Figure 2). Alkali basalt and basanites/tephrites primarily consist of olivines, clinopyroxenes, and Fe-Ti oxides (Figures 2d–2g). We observe more samples with olivine content above 10% and therefore in further text we refer to basanites/tephrites as basanites only. Euhedral clinopyroxenes, amphiboles, and subordinate plagioclases, followed by Fe-Ti oxides, are dominant phenocrysts of mugearites and phono-tephrites (Figures 2h and 2i). In contrast, most phenocrysts in benmoreites are euhedral plagioclase with subordinate clinopyroxene, amphibole, Fe-Ti oxides, and h aüyne (Figures 2j–2l). Phenocrysts in all samples are set in a glassy hypocrystalline groundmass with intersertal and fluidal textures, consisting of plagioclases with subordinate clinopyroxenes, amphiboles, and Fe-Ti oxides microliths, except for an aphyric sample (mugearite (9A) Figure 2b). Sporadic apatites and sulfides are found in mugearites, phono-tephrites, and benmoreites. H aüyne, a feldspathoid of the sodalite group, is here reported in the Vesteris rock suite for the first time (Figure 2k). Although common in alkaline volcanic rocks

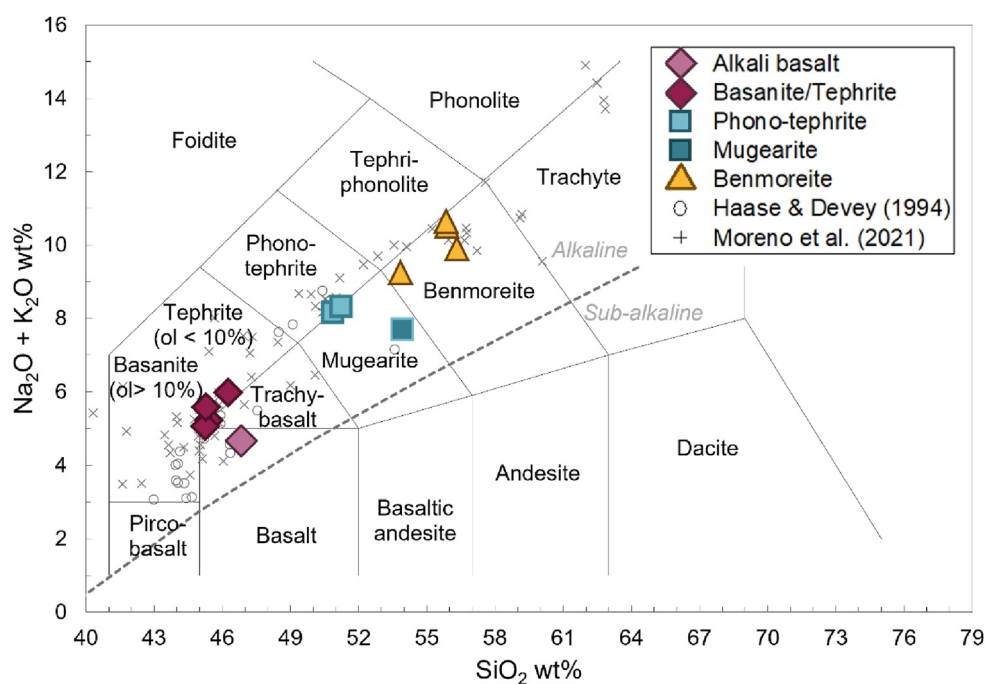


Figure 3. The Total Alkali versus Silica (wt%) classification diagram (TAS; Le Maitre et al., 2002) shows the compositional range re-calculated on a dry basis of the investigated 12 volcanic rocks from Vesteris Seamount (Table S1). All rocks are alkaline and sodic (alkaline-sub-alkaline discrimination line after Irvine & Baragar, 1971). Vesteris samples from this study are shown with large symbols, color-coded following petrographic and chemical grouping: alkali basalt/basanites (pink diamonds), mugearite/phono-tephrites (blue squares), and benmoreites (yellow triangles). Data from other studies for Vesteris Seamount are shown with gray symbols (K. M. Haase & Devey, 1994; Moreno et al., 2021).

(i.e., Cooper et al., 2015; Melluso et al., 2018, 2021), the NE Atlantic h aüyne was previously reported only in tephrites of the nearby Southern Seamount (Chernysheva & Kharin, 2007). Fractured phenocrysts and glass embayments suggest fast ascent, emplacement, and rapid growth. Clinopyroxene, amphibole, and plagioclase phenocrysts show oscillatory and sector zoning, indicating magma mixing or mingling. Melt inclusions are abundant in olivine, clinopyroxene, amphibole, and h aüyne but rare in plagioclase.

4.2. Whole-Rock Geochemical Compositions

4.2.1. Degree of Seawater Alteration

Long-term interaction with seawater has not resulted in any significant degree of hydration of our selected samples (LOI < 1.12 wt%) and does not appear to have mobilized any of the major and trace elements. For instance, when major and trace elements are plotted as a function of an immobile element such as TiO₂, there is no systematic loss of CaO and MgO coupled to any gain in U, Ba, K₂O, SiO₂, and Rb (e.g., Alt, 1995; Donnelly et al., 1980; Revillon et al., 2007; Staudigel et al., 1996). There is also no correlation between the LOI index and mobile elements (Sr, Rb, Ba, e.g., Sayyed, 2014).

4.2.2. Major and Trace Elements

Major and trace element concentrations of Vesteris rocks are presented in Data Table S1. In the diagram of Total Alkali versus Silica diagram (TAS; Le Maitre et al., 2002), Vesteris samples (*N* = 12) are classified as basanites (93D-14, 34, 47; 94D-2), alkali basalt (93D-15), phono-tephrites (93D-7, 10), mugearite (sodic basaltic trachyandesites; 93D-9A), and benmoreites (sodic trachyandesites; 93D-1, 6, 13, 28). The analyzed lava samples belong to the sodic alkaline magma series (Na₂O – 2.0 > K₂O) (Figure 3). They range from relatively primitive to mildly evolved rocks, with MgO content ranging from 4.99 to 10.46 wt% for basanites and alkali basalts, 2.73 to 3.24 wt% for mugearites and phono-tephrites and 1.48 to 2.06 wt% for benmoreites (Figure 4). As a function of MgO concentration, the major element variations of Vesteris samples define systematic compositional trends going from basanites and alkali basalts to phonotephrites and mugearites

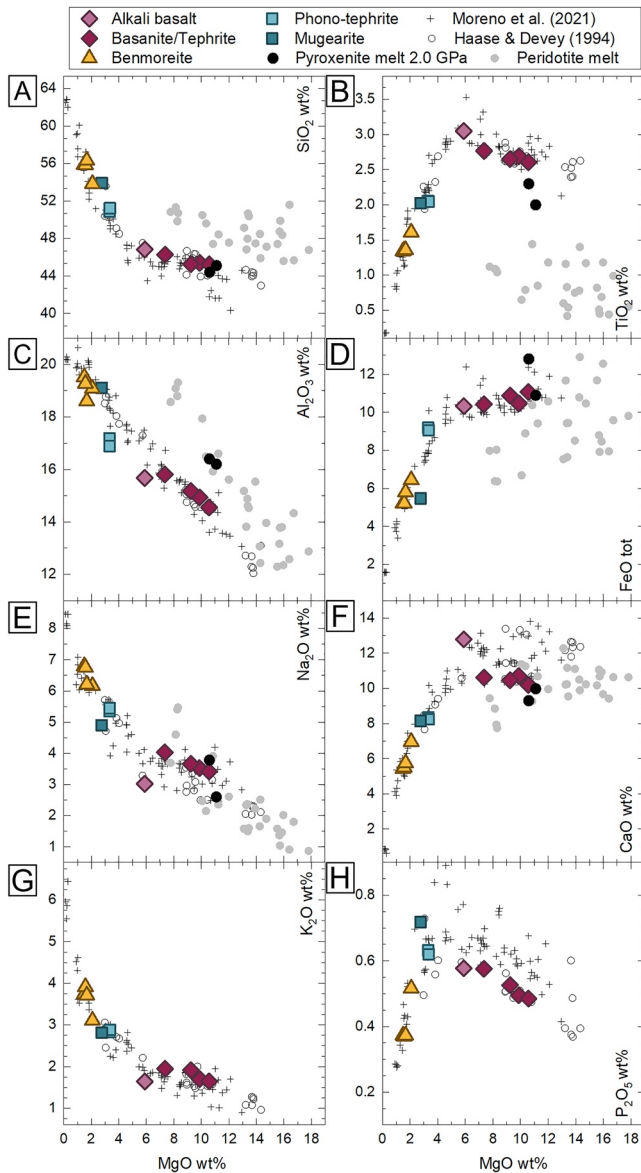


Figure 4. Major element variation (wt%) versus MgO (wt%) diagrams of Vesteris Seamount lavas. Symbols as in Figure 3. MgO content ranges from 4.99 to 10.46 wt% for alkali basalt and basanites, 2.73 to 3.24 wt% for mugearites and phono- tephrites, and 1.48 to 2.06 wt% for benmoreites. SiO_2 , Al_2O_3 , Na_2O , and K_2O increase with decreasing MgO concentration. Sharp kinks of TiO_2 , P_2O_5 , and CaO at ca. 4–6 wt% MgO are attributed to oxide, apatite, clinopyroxene, and plagioclase fractionation. Glasses from partial melting experiments are plotted for comparison; garnet pyroxenite MIX1G (2.0 GPa) (Hirschmann et al., 2003) and anhydrous peridotite HK-66 (2–5 GPa) (Hirose & Kushiro, 1993).

to benmoreites, with Al_2O_3 , Na_2O , and K_2O increasing with decreasing MgO concentration (Figure 4). The alkali basalt sample is slightly shifted toward lower Al_2O_3 , Na_2O , and K_2O relative to the general trends defined by the Vesteris samples. Phono-tephrites and mugearites show shifts from general trends toward lower Al_2O_3 and Na_2O , FeO , and P_2O_5 . As MgO decreases, the increase in TiO_2 , P_2O_5 , and CaO shows sharp kinks at ca. 4–6 wt% MgO, from which these elements sharply drop. The substantial decrease in P_2O_5 and CaO at less than <4 wt% MgO reflects the appearance of apatite on the liquidus. The onset of Fe-Ti oxide fractionation is marked by a decline in TiO_2 at <4 wt%. The greater scatter observed for the most differentiated rocks can be attributed to the variable accumulation of phenocrysts.

Compatible trace element concentrations, such as Sc, Cr, Ni, and Co, decrease with fractionation degree (decreasing MgO), with primitive basanites having the highest concentrations (Sc = 31 ppm, Cr = 488 ppm, Ni = 251 ppm, Co = 55 ppm; Figure 5). Highly to moderately incompatible trace element concentrations (e.g., Ba, Nb, Sr, Y), show an overall increase with decreasing MgO (Figure 5). These elements show a negative correlation with MgO in lava samples with MgO <4 wt%, likely due to a fractionating assemblage of plagioclase, fractionation of apatite and kaersutitic amphibole.

The REE patterns (normalized to chondrite, McDonough & Sun, 1995) show strong similarities to typical ocean island basalts (OIB-type) but are slightly more enriched in the most incompatible elements (Figure 6a; McDonough & Sun, 1995). They show a high fractionation of light REE (LREE) relative to heavy REE (HREE) but with a steeper LREE slope (Figure 6a). Basaltic lavas from Jan Mayen, off-axis Iceland, and East Greenland post-breakup magmatism south of Scoresby Sund also show these characteristics (Jensen, 1998; Thirlwall et al., 1994; Trønnes et al., 1999). Both ratios of LREE relative to HREE or middle REE (MREE) increase with differentiation ($(\text{La}/\text{Yb})_{\text{CH}}$ = ca. 16.59 (alkali basalt); ca. 23.25 (mugearite); ca. 28.97 (benmoreites) (Figure 6a)).

Primitive mantle normalized (Sun & McDonough, 1989) incompatible trace elements show patterns partially overlapping with those of OIB (Sun & McDonough, 1989). There is a broad similarity in most HFSE (High field strength elements) and HREE. Still, our lava samples are much more enriched in LILE and Th, U, Na, and Ta (Figure 6b). All samples have primitive mantle-normalized incompatible element patterns with positive Nb and Ta anomalies typical of within-plate volcanic rocks, including OIB (Willbold & Stracke, 2006). All the analyzed samples share negative K anomalies. A negative Ti anomaly increases with the differentiation, which is most prominent in benmoreites. Also, positive anomalies in Th, U, and Pb are stronger for the phono-tephrites and mugearites, likely reflecting apatite and plagioclase accumulation. Patterns of basanites and benmoreites are broadly parallel with each other but show some variability (Ba = 79–189 ppm, U = 80–326 ppm, La = 76–188, Yb = 4–6) (Figure 6b). Phonotephrites lie above the arrays defined by basanites and benmoreites, having higher Ba, Nd, Sr, Hf, Sm, Eu, and HREE (Figure 6b). We observe a significant spread in Ba and Sr for phonotephrites 7, 10, mugearites 9A, and benmoreite 28, possibly explained by varying levels of fractionation and accumulation of plagioclase and possible amphibole fractionation. This is indicated by a negative Ba anomaly in benmoreites compared to La values, as Sr and Ba can be compatible elements in plagioclase (McKenzie & O’Nions, 1991) and amphibole (Chazot et al., 1996).

to benmoreites, with Al_2O_3 , Na_2O , and K_2O increasing with decreasing MgO concentration (Figure 4). The alkali basalt sample is slightly shifted toward lower Al_2O_3 , Na_2O , and K_2O relative to the general trends defined by the Vesteris samples. Phono-tephrites and mugearites show shifts from general trends toward lower Al_2O_3 and Na_2O , FeO , and P_2O_5 . As MgO decreases, the increase in TiO_2 , P_2O_5 , and CaO shows sharp kinks at ca. 4–6 wt% MgO, from which these elements sharply drop. The substantial decrease in P_2O_5 and CaO at less than <4 wt% MgO reflects the appearance of apatite on the liquidus. The onset of Fe-Ti oxide fractionation is marked by a decline in TiO_2 at <4 wt%. The greater scatter observed for the most differentiated rocks can be attributed to the variable accumulation of phenocrysts.

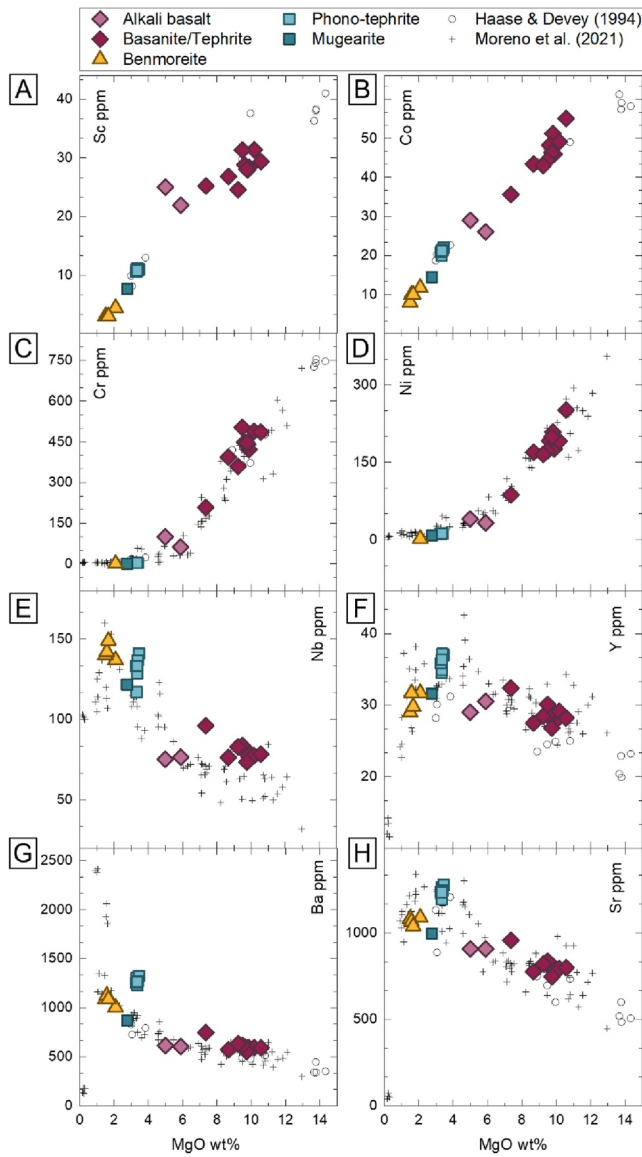


Figure 5. Trace element variations (ppm) versus MgO (wt%) diagrams of Vesteris Seamount lavas. Compatible trace element concentrations decrease significantly with fractionation degree, with primitive basanites having the highest concentrations (Sc = 31 ppm, Cr = 488 ppm, Ni = 251 ppm, Co = 55 ppm). Highly to moderately incompatible trace element concentrations (e.g., Ba, Nb, Sr, Y) show an overall negative correlation; phonotephrites are outliers regarding Ba and Sr concentrations.

4.3. Isotopic Compositions

This study presents new Sr, Nd, and Pb isotopic compositions for Vesteris whole-rock samples ($N = 12$), along with the first Hf isotope compositions ever obtained on samples from this seamount (Table S1; Figure 7; Figures S2–S4 in Supporting Information S1). Previously published data on volcanic rocks from the region are integrated in Figure 7 for comparison (Bernstein et al., 2000; Blichert-Toft et al., 2005; Elkins et al., 2014, 2016; K. M. Haase et al., 1996; Hards et al., 1995; Harðardóttir et al., 2022; Jensen, 1998; Kokfelt et al., 2006, 2009; Manning & Thirlwall, 2014; Mertz & Haase, 1997; Peate et al., 2010; Prestvik et al., 2001; Schilling et al., 1999; Storey et al., 2004; Thirlwall et al., 1994; Trønnes et al., 1999). As a whole, our samples define restricted isotopic variability.

The Hf isotopic compositions of the samples cluster between ($^{176}\text{Hf}/^{177}\text{Hf} = 0.283139\text{--}0.283156$; $\epsilon_{\text{Hf}} = +12.51$ to $+13.12$), while the Nd isotopic compositions range between ($^{143}\text{Nd}/^{144}\text{Nd} = 0.512931\text{--}0.512965$; $\epsilon_{\text{Nd}} = +5.88$ to $+6.52$). $^{87}\text{Sr}/^{86}\text{Sr}$ ranges between 0.703576 and 0.703733. Pb isotopic signatures range between 18.656 and 18.723 in $^{206}\text{Pb}/^{204}\text{Pb}$, 15.506 and 15.516 in $^{207}\text{Pb}/^{204}\text{Pb}$, and 38.518 and 38.638 in $^{208}\text{Pb}/^{204}\text{Pb}$.

In the $^{207}\text{Pb}/^{204}\text{Pb}$ versus $^{206}\text{Pb}/^{204}\text{Pb}$ isotopic space, Vesteris lavas overlap the Northern Hemisphere Reference Line (NHRL; Hart, 1984), with only a slightly negative $\Delta 7/4$ value (average value: -0.52), respectively ($\Delta 7/4$ is the offset of $^{207}\text{Pb}/^{204}\text{Pb}$ relative to the Northern Hemisphere reference line at a given $^{206}\text{Pb}/^{204}\text{Pb}$, as defined by $^{207}\text{Pb}/^{204}\text{Pb} = 0.1084 (^{206}\text{Pb}/^{204}\text{Pb}) + 13.491$; Hart, 1984). In the $^{208}\text{Pb}/^{204}\text{Pb}$ versus $^{206}\text{Pb}/^{204}\text{Pb}$ isotopic space, Vesteris lavas plot well above NHRL with positive $\Delta 8/4$ values (average value: 34.35; $\Delta 8/4$ is the offset of $^{208}\text{Pb}/^{204}\text{Pb}$ relative to the Northern Hemisphere reference line at a given $^{206}\text{Pb}/^{204}\text{Pb}$, as defined by $^{208}\text{Pb}/^{204}\text{Pb} = 1.209 (^{206}\text{Pb}/^{204}\text{Pb}) + 15.627$ (Hart, 1984) (Figure 7); Figures S3 and S4 in Supporting Information S1).

Our new Sr-Nd-Pb isotope data form a tight cluster and broadly overlap with previously published data for Vesteris (Mertz & Haase, 1997). Within our sample set, alkali basalt, mugearite, and phono-tephrites have slightly lower $^{143}\text{Nd}/^{144}\text{Nd}$ (<0.512960) compared to basanites/tephrites and benmoreites (Figure S2 in Supporting Information S1). The phono-tephrites and the mugearite also have the highest $^{206}\text{Pb}/^{204}\text{Pb}$ and $^{208}\text{Pb}/^{204}\text{Pb}$ ratios (Figure S2 in Supporting Information S1) (e.g., phono-tephrite (18.722 and 38.638) and mugearite (18.694 and 38.594), respectively).

5. Discussion

5.1. Vesteris Isotopes in the Context of NE Atlantic Signatures

In the Sr-Nd isotopic space (Figure 7a), Vesteris samples plot within the mantle array (DePaolo & Wasserburg, 1979). Regionally, they plot distinctly bottom-right of the North Atlantic MORBs field (Reykjanes, Kolbeinsey, Mohn's, Knipovich, and partially Gakkell Ridge) having less radiogenic $^{143}\text{Nd}/^{144}\text{Nd}$, and more radiogenic $^{87}\text{Sr}/^{86}\text{Sr}$. They fall at the enriched end of the IP field (Fitton et al., 2003; Kempton et al., 2000; Kokfelt et al., 2006; Peate et al., 2010; Thirlwall et al., 2004). Vesteris lavas cluster at higher $^{87}\text{Sr}/^{86}\text{Sr}$ and $^{143}\text{Nd}/^{144}\text{Nd}$ than most samples from Jan Mayen Island (Trønnes et al., 1999). Compared with the Jan Mayen Platform, Vesteris lavas have comparable $^{143}\text{Nd}/^{144}\text{Nd}$ but exhibit similar to slightly higher $^{87}\text{Sr}/^{86}\text{Sr}$ values (Blichert-Toft et al., 2005; Elkins et al., 2016; Trønnes et al., 1999). Our Vesteris data differ from most of Iceland, being more radiogenic in $^{87}\text{Sr}/^{86}\text{Sr}$ and extending toward less radiogenic $^{143}\text{Nd}/^{144}\text{Nd}$, except for some samples from the South Iceland Volcanic Zone that have less radiogenic $^{143}\text{Nd}/^{144}\text{Nd}$. Our alkali basalt and mugearites from Vesteris overlap with the Örafajökull cluster,

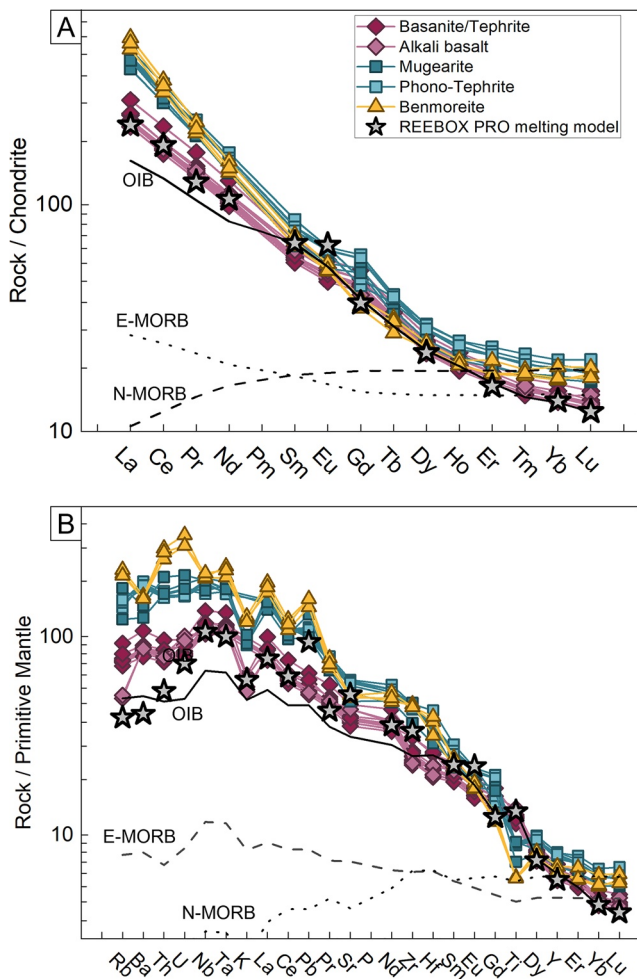


Figure 6. (a) Chondrite normalized (McDonough & Sun, 1995) Rare-Earth Element patterns of Vesteris Seamount (basalts: pink, mugearites, phono-tephrites: blue, and benmoreites: yellow) in comparison with N-MORB, E-MORB, and OIB (McDonough & Sun, 1995). (b) Primitive mantle-normalized (Sun & McDonough, 1989) multi-element diagrams illustrate trace element compositions of Vesteris Seamount in comparison with N-MORB, E-MORB, and OIB (Sun & McDonough, 1989). Using the REEBOX PRO melting model, melt compositions of Vesteris seamount are roughly reproduced by 3%–4% melting under a pre-existing lithosphere of 65 km of a bimodal source composition composed of 50% anhydrous peridotite (PYROLITE) bearing a primitive mantle trace element composition (McDonough & Sun, 1995) and 50% silica undersaturated pyroxenite MIX1G having an N-MORB trace element composition (Sun & McDonough, 1989).

while the other Vesteris samples fall between the eastern Iceland flank zone (Öræfajökull-Snaefell) and Jan Mayen compositions (Chekol et al., 2011; Kokfelt et al., 2006; Peate et al., 2010; Prestvik et al., 2001; Thirlwall et al., 2004) (Figure 7 and Figure S3 in Supporting Information S1).

In the ϵNd - ϵHf space, Vesteris samples plot above the mantle array ($\epsilon\text{Hf} = 1.44 \epsilon\text{Nd} + 1.61$; Chauvel et al., 2008; Jones et al., 2019; Vervoort et al., 2011); in the fields defined by Atlantic MORB and OIB. When compared with the Iceland field (Harðardóttir et al., 2022), Vesteris lavas plot near its unradiogenic end, along with Snaefell (Peate et al., 2010) and Öræfajökull samples (Prestvik et al., 2001) (Figure 7), even if the Öræfajökull compositional cluster extends toward lower ϵHf values. Vesteris rocks show more radiogenic ϵHf - ϵNd values than Jan Mayen Island but lie within the trend defined by Jan Mayen Platform samples, located near the southern termination of Mohn's Ridge. Some of the latter rocks are more radiogenic in ϵHf than Vesteris (Blichert-Toft et al., 2005).

In Pb-Pb isotopic spaces, Vesteris samples form a single cluster (Figures 7c and 7d). In $^{207}\text{Pb}/^{204}\text{Pb}$ versus $^{206}\text{Pb}/^{204}\text{Pb}$, they fall slightly below the NHRL (avg. $\Delta 7/4 = -0.58$) but above the trend defined by most Atlantic MORBs and Jan Mayen (island and platform; Kokfelt et al., 2006, 2009; Manning & Thirlwall, 2014; Peate et al., 2010; Prestvik et al., 2001; Trønnes et al., 1999) and Mohn's Ridge. Here, Vesteris samples plot at an intermediate position between the main Icelandic array and samples from Öræfajökull, which cluster near NHRL. There is still partial overlap with Öræfajökull compositions, but less pronounced than what is observed for the other isotopic systems. An even more pronounced shift toward positive $\Delta 7/4$ values is a characteristic of Tertiary magmatism occurring at the Northeastern Greenland Margin (NEGM), north from Scoresby Sund at Wollaston Forland, Hold with Hope, Kap Simpson, and Werner Bjerge. The isotopic signatures of this magmatism have been attributed to remobilization of moderately radiogenic lead from local, continental crust; basement and sedimentary basins (Palaeoproterozoic-Mesoproterozoic gneisses, Neoproterozoic-Ordovician sediments, Caledonian granites, and Palaeozoic-Mesozoic sediments; Thirlwall et al., 1994; Jensen, 1998).

In the $^{208}\text{Pb}/^{204}\text{Pb}$ versus $^{206}\text{Pb}/^{204}\text{Pb}$ diagram, Vesteris samples lie well above the NHRL and slightly above the array delineated by most Atlantic MORBs and lavas from Jan Mayen (island and platform; Kokfelt et al., 2006, 2009; Manning & Thirlwall, 2014; Peate et al., 2010; Prestvik et al., 2001; Trønnes et al., 1999) and Mohn's ridge. The strong positive $\Delta 8/4$ (avg. 34.35) of Vesteris samples is comparable to that of Öræfajökull, NEGM Tertiary basalts, and to some samples of Jan Mayen Island and Platform (Trønnes et al., 1999).

In summary, the observed overlap in isotope trends between high latitude North Atlantic MORBs signatures (53° – $73^\circ 30' \text{N}$) and the Iceland array indicates a common genetic relationship between these two magmatic realms. A two-end-member control on the Arctic Ocean and North Atlantic magmatism mainly produces such a trend. The Sr-Nd-Pb isotopic variability of magmas from these areas is most easily explained by mixing the depleted mantle (DM) and enriched plume material (IP; Mertz & Haase, 1997).

In the Pb-Pb space (Figures 7c and 7d), Vesteris $^{206}\text{Pb}/^{204}\text{Pb}$ compositions plot along this main trend, and in this sense, they reflect the regional picture of isotopic signatures as a mixture between a plume and a depleted source component. However, together with samples from Öræfajökull-Snaefell flank zones, and to some extent samples from Jan Mayen, Vesteris $^{207}\text{Pb}/^{204}\text{Pb}$, $^{208}\text{Pb}/^{204}\text{Pb}$, and ϵHf are shifted away from this main trend, asking for an additional component to their mantle source (Figure 7, Mertz & Haase, 1997).

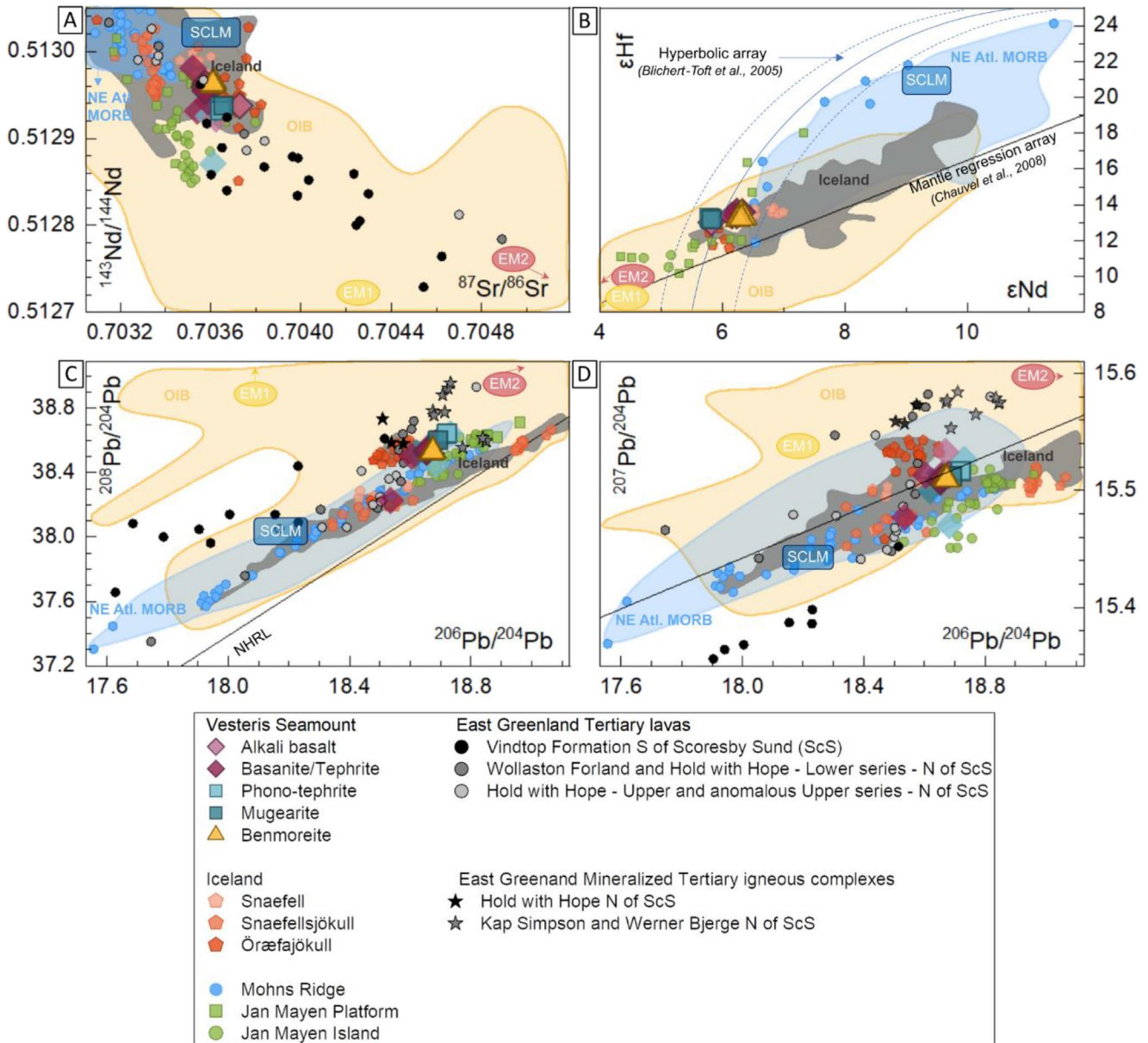


Figure 7. Sr-Nd-Pb-Hf isotopic compositions of Vesteris Seamount and neighboring volcanic occurrences. Vesteris samples analyzed in this study are presented with thick edges, while samples studied by Mertz and Haase (1997) from Vesteris plotted here for comparison are presented without an edge. (a) $^{87}\text{Sr}/^{86}\text{Sr}$ - $^{143}\text{Nd}/^{144}\text{Nd}$, (b) ϵHf versus ϵNd (ϵHf and ϵNd calculated by CHUR values by Dickin (2018)); mantle array described by $\epsilon\text{Hf} = 1.44 \epsilon\text{Nd} + 1.61$ (Chauvel et al., 2008; Jones et al., 2019; Vervoort et al., 2011), (c) $^{208}\text{Pb}/^{204}\text{Pb}$ - $^{206}\text{Pb}/^{204}\text{Pb}$ (Northern hemisphere reference line described by $^{207}\text{NHRL} = 0.1084 (^{206}\text{Pb}/^{204}\text{Pb}) + 13.491$; Hart, 1984) and (d) $^{208}\text{Pb}/^{204}\text{Pb}$ - $^{206}\text{Pb}/^{204}\text{Pb}$ (NHRL described by $^{208}\text{NHRL} = 1.209 (^{206}\text{Pb}/^{204}\text{Pb}) + 15.627$; Hart, 1984). Isotope ratios of mantle components EM1 and EM2 and approximate directions are given for each plot. Components are represented as averages of Pitcairn (EM1; $^{143}\text{Nd}/^{144}\text{Nd} = 0.512692$; $^{87}\text{Sr}/^{86}\text{Sr} = 0.704115$; $^{206}\text{Pb}/^{204}\text{Pb} = 18.148$; $^{207}\text{Pb}/^{204}\text{Pb} = 15.501$; $^{208}\text{Pb}/^{204}\text{Pb} = 38.900$; $\epsilon\text{Hf} = -2.55$; $\epsilon\text{Nd} = +1.21$) and Samoa (EM2; $^{143}\text{Nd}/^{144}\text{Nd} = 0.512742$; $^{87}\text{Sr}/^{86}\text{Sr} = 0.705635$; $^{206}\text{Pb}/^{204}\text{Pb} = 19.036$; $^{207}\text{Pb}/^{204}\text{Pb} = 15.603$; $^{208}\text{Pb}/^{204}\text{Pb} = 39.227$; $\epsilon\text{Hf} = +4.53$; $\epsilon\text{Nd} = +1.21$) (Supplementary Table 1 in Stracke, 2012). The mean value for sub-continental lithospheric mantle component is calculated from the isotopic compositions of lherzolite, harzburgite, clinopyroxene and amphibole xenoliths from Spitsbergen Island ($\epsilon\text{Hf} = +61.11 \pm 45.72$; $\epsilon\text{Nd} = +8.44 \pm 3.94$, Choi et al., 2010); Sr-Nd-Pb data ($^{87}\text{Sr}/^{86}\text{Sr} = 0.70363 \pm 0.00039$; $^{143}\text{Nd}/^{144}\text{Nd} = 0.51301 \pm 0.0003$; $^{206}\text{Pb}/^{204}\text{Pb} = 18.23 \pm 0.31$; $^{207}\text{Pb}/^{204}\text{Pb} = 15.44 \pm 0.05$; $^{208}\text{Pb}/^{204}\text{Pb} = 38.06 \pm 0.32$, Ionov et al., 2002). The transparent blue and yellow background shows NE Atlantic MORB and OIB fields (Supplementary Table 1 in Stracke, 2012). Iceland database is shown with a gray background (Iceland IVID database, Harðardóttir et al., 2022). Data sources: Vesteris Seamount (Mertz & Haase, 1997); East Greenland lavas N of Scoresby Sund (Jensen, 1998; Thirlwall et al., 1994); East Greenland lavas S of Scoresby Sund (Bernstein et al., 2000; Storey et al., 2004); Jan Mayen (Elkins et al., 2016; Trønnes et al., 1999); Iceland (IVID data set; Harðardóttir et al., 2022); Iceland flank zones: Öræfajökull and Snaefall (Manning & Thirlwall, 2014; Peate et al., 2010; Prestvik et al., 2001); Snaefellsjökull (Hards et al., 1995; Kokfelt et al., 2006, 2009); Mohn's Ridge (Blichert-Toft et al., 2005; Elkins et al., 2016; K. M. Haase et al., 1996; Schilling et al., 1999).

5.2. Vesteris Seamount Source End-Members

We use our isotopic data to evaluate the nature and contribution of different source end-members to the petrogenesis of Vesteris magmas (Figure 8). Excluding the Tertiary lavas, the samples from the NE Atlantic broadly define a triangular shape in $^{207}\text{Pb}/^{204}\text{Pb}$ - $^{206}\text{Pb}/^{204}\text{Pb}$. The apexes of this compositional triangle correspond to (a) the unradiogenic Mohn's Ridge MORB; (b) the most radiogenic $^{206}\text{Pb}/^{204}\text{Pb}$ end-member below the NHRL, defined by South Iceland Volcanic Zone; (c) an intermediate $^{206}\text{Pb}/^{204}\text{Pb}$ end-member, but accompanied by high $^{207}\text{Pb}/^{204}\text{Pb}$, defined by Öraefajökull. Vesteris samples plot within this triangular distribution, which reflects the presence of at least three source components. We first focus on two of these components, that is, the regional depleted and enriched mantle end-members, their signatures, and their origin. Afterward, we discuss the contribution of additional enriched sources that may explain our geochemical results.

5.2.1. Depleted mantle (DM): The Depleted End-Member

The best candidate for the depleted end-member component at regional scale is represented by the Sr-Nd-Pb isotopic composition of a Mohn's MORB sample (Sample EN26 32D-3g; Table 1a in Schilling et al., 1999; Blichert-Toft et al., 2005), characterized by a low $^{206}\text{Pb}/^{204}\text{Pb}$ (17.927), $^{207}\text{Pb}/^{204}\text{Pb}$ (15.417), $^{208}\text{Pb}/^{204}\text{Pb}$ (37.570), $^{87}\text{Sr}/^{86}\text{Sr}$ (0.703173) and high $^{176}\text{Hf}/^{177}\text{Hf}$ (0.283401) and $^{143}\text{Nd}/^{144}\text{Nd}$ (0.513083) (Figure 8, Table S2). We ascribe to this end-member the Pb concentration of the DM (0.018 ppm) defined by Workman and Hart (2005).

5.2.2. Main Iceland Plume (IP): The Enriched End-Member

Basalts from Iceland show a wide range of compositions. The elongated trends below the NHRL described by Icelandic rocks (IVID database, Harðardóttir et al., 2022) in the $^{207}\text{Pb}/^{204}\text{Pb}$ - $^{206}\text{Pb}/^{204}\text{Pb}$ space and above the NHRL in the $^{208}\text{Pb}/^{204}\text{Pb}$ - $^{206}\text{Pb}/^{204}\text{Pb}$ space, require a component with high radiogenic $^{206}\text{Pb}/^{204}\text{Pb}$ (>18.8) and one with low-radiogenic $^{206}\text{Pb}/^{204}\text{Pb}$ (<18.8). Low radiogenic picrites ($^{206}\text{Pb}/^{204}\text{Pb} < 18.1$; Eastern and Northern Rift Zone in Harðardóttir et al., 2022) from the North and East Rift Zones were interpreted as entrained MORB-source mantle into the rising IP (Elliott et al., 1991). Conversely, the radiogenic compositions ($^{206}\text{Pb}/^{204}\text{Pb} > 18.8$) recorded in the South Iceland Volcanic Zone, paired with one of the highest $^3\text{He}/^4\text{He}$ isotope ratios observed in the area (ca. 17–22 R_A ; Harðardóttir et al., 2022; Starkey et al., 2009), are thought to represent the HIMU-ROC (recycled oceanic crust) IP component (Stecher et al., 1999; Torsvik et al., 2015). Many studies support the notion that the enriched IP domains bear the signature of recycled oceanic crust (i.e., Fitton et al., 1997; Hemond et al., 1993; Hofmann & White, 1982; Sobolev et al., 2000). Thus, it is difficult to describe the IP isotopic flavor with a univocal signature because the wide range of Sr-Nd-Pb isotopic values measured on IP-derived magmas suggest the presence of both refractory and fertile components in the IP itself (Dasgupta et al., 2010; Stracke, 2012). We here refer to IP signature as a composition that can represent the enriched end-member of the Iceland and North Atlantic MORB array, that is, high $^{206}\text{Pb}/^{204}\text{Pb}$ (19.239) with a moderate $^{207}\text{Pb}/^{204}\text{Pb}$ (15.550), $^{208}\text{Pb}/^{204}\text{Pb}$ (38.832), and $^{143}\text{Nd}/^{144}\text{Nd}$ (0.512976) and $^{87}\text{Sr}/^{86}\text{Sr}$ (0.703275), and low $^{176}\text{Hf}/^{177}\text{Hf}$ (0.283086), as exemplified, for instance, by Sample BHE-43 from South Iceland Volcanic Zone (Harðardóttir et al., 2022) (Figure 8). For this end-member, we chose the Pb concentration of the primitive mantle (0.185 ppm; Sun & McDonough, 1989).

Vesteris rocks have moderate $^{206}\text{Pb}/^{204}\text{Pb}$ (18.656–18.723) compositions within the range of the Iceland and North Atlantic MORB array (Figures 7c and 7d). Hence, the $^{206}\text{Pb}/^{204}\text{Pb}$ position of Vesteris Seamount along this array is best reproduced by binary mixing of the two end-member components just described (Figure 8, Table S2). The unradiogenic lead component represented by a sample from Mohn's ridge (Sample EN26 32D-3g; Schilling et al., 1999) contributes between 85% and 90%, and the IP end-member with more radiogenic lead, represented by lava from the South Iceland Volcanic Zone (Sample BHE-43; Harðardóttir et al., 2022) contributes between 10% and 15% (Table S2). A variable range of these contributions best explains the variation in $^{206}\text{Pb}/^{204}\text{Pb}$ signatures in the Vesteris data set. However, as noted above, a third component is shifting Vesteris samples toward higher $^{207}\text{Pb}/^{204}\text{Pb}$ and $^{208}\text{Pb}/^{204}\text{Pb}$ (Figure 8.) at a given $^{206}\text{Pb}/^{204}\text{Pb}$ with respect to the regional Iceland and NE Atlantic MORB array.

5.2.3. Crustal Component

5.2.3.1. Crustal Component in the Source

The Sr-Nd-Hf and Pb isotopic compositions of Vesteris samples share similarities with those of lavas from Iceland flank zones (Öraefajökull-Snaefell; Manning & Thirlwall, 2014), which are anomalous when compared

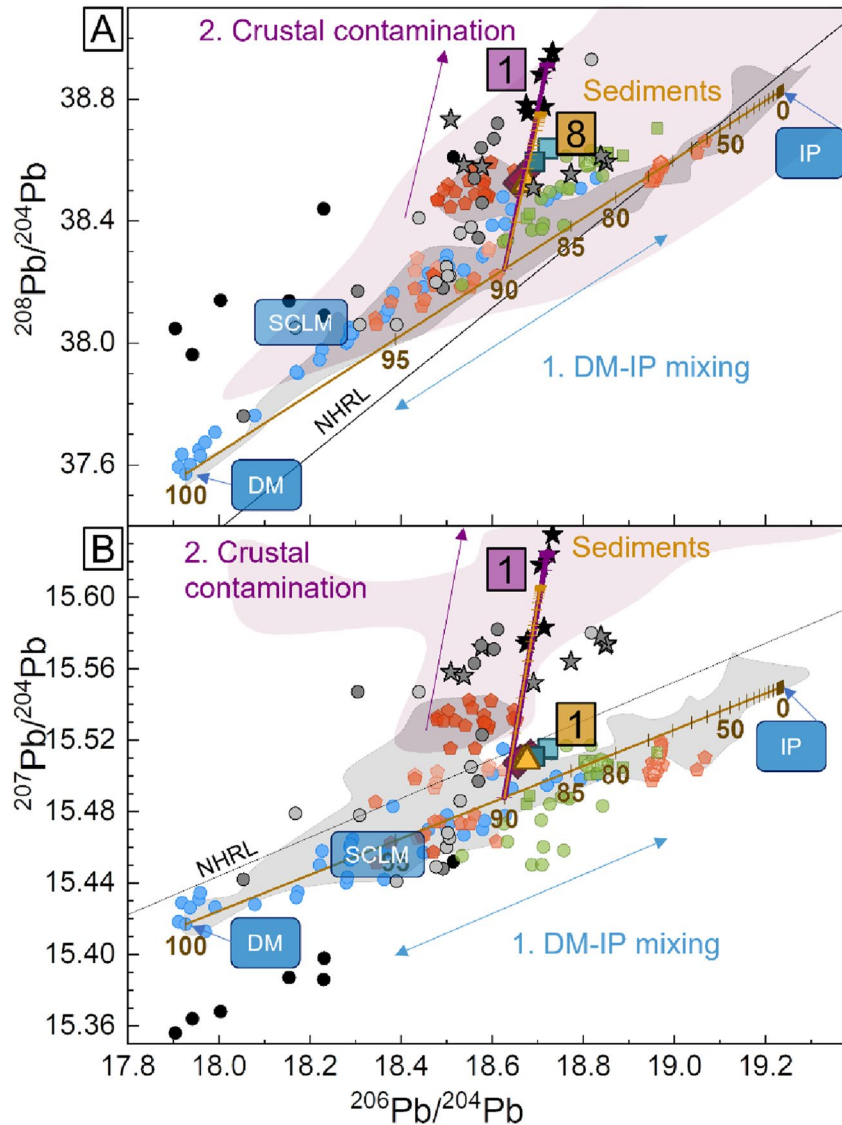


Figure 8. Mixing model of proposed crustal contamination for Vesteris Seamount basalts shown on Pb-isotopic diagrams. (a) $^{207}\text{Pb}/^{204}\text{Pb}$ - $^{206}\text{Pb}/^{204}\text{Pb}$ and (b) $^{208}\text{Pb}/^{204}\text{Pb}$ - $^{206}\text{Pb}/^{204}\text{Pb}$ diagram, showing the proposed mixing model (Table S2). In the mixing model, we refer only to the Vesteris samples analyzed in this study, with state-of-the-art precision, forming a uniform cluster. Legend is as in Figure 7. All values used in the mixing model are presented in data Table S2. A three-component mixture can explain Vesteris lavas compositions. First, a binary mixing trend extends from a depleted end-member (shallow mantle, resembling the depleted mantle (DM)) and an enriched end-member (deep mantle, resembling the Iceland Plume—IP). The depleted end-member composition, labeled as DM, with low $^{206}\text{Pb}/^{204}\text{Pb}$ (17.927), $^{207}\text{Pb}/^{204}\text{Pb}$ (15.417), $^{208}\text{Pb}/^{204}\text{Pb}$ (37.570), $^{87}\text{Sr}/^{86}\text{Sr}$ (0.703173) and high $^{176}\text{Hf}/^{177}\text{Hf}$ (0.283401), and $^{143}\text{Nd}/^{144}\text{Nd}$ (0.513083) is taken from sample EN26 32D-3g (Table 1a in Schilling et al., 1999; Blichert-Toft et al., 2005). For this end-member, we chose the Pb concentration of the DM (0.018 ppm; Workman & Hart, 2005). The enriched end-member is characterized by these Sr-Nd-Hf-Pb isotopic ratios: $^{206}\text{Pb}/^{204}\text{Pb}$ (19.239), $^{207}\text{Pb}/^{204}\text{Pb}$ (15.550), $^{208}\text{Pb}/^{204}\text{Pb}$ (38.832), $^{143}\text{Nd}/^{144}\text{Nd}$ (0.512976), $^{87}\text{Sr}/^{86}\text{Sr}$ (0.703275) and $^{176}\text{Hf}/^{177}\text{Hf}$ (0.283086). Its composition is taken from the BHE-43 sample in the South Iceland Volcanic Zone (Harðardóttir et al., 2022). For this end-member, we chose the Pb concentration of the primitive mantle (0.185 ppm; Sun & McDonough, 1989). Then, another trend is calculated from a mixture of 85%–90% DM and 10%–15% IP composition along this line and a continental contaminant with higher $^{207}\text{Pb}/^{204}\text{Pb}$ and $^{208}\text{Pb}/^{204}\text{Pb}$. The latter contaminant is taken as an average of three clustered samples with the highest $^{207}\text{Pb}/^{204}\text{Pb}$ and $^{208}\text{Pb}/^{204}\text{Pb}$ from Malmberg in the WB alkaline complex (average of three samples; $^{206}\text{Pb}/^{204}\text{Pb}$ (18.722); $^{207}\text{Pb}/^{204}\text{Pb}$ (15.626); $^{208}\text{Pb}/^{204}\text{Pb}$ (38.919) (Table S2) (Jensen, 1998)). For the Pb concentration, we use 42 ppm, the average of 250 pre-Tertiary rocks from Gauss Halvø, Hudson Land, and Kuhn Ø as compiled by Jensen (1998). Up to 1% of this contaminant is sufficient to account for the compositions of Vesteris samples. Alternatively, sediments (pink field) as another possible continental contaminant with elevated $^{207}\text{Pb}/^{204}\text{Pb}$ and $^{208}\text{Pb}/^{204}\text{Pb}$ ratios, are taken into consideration, namely the Haltenbanken sediments (Torsvik et al., 2015). We chose a sample from the Haltenbanken sediments compilation; $^{206}\text{Pb}/^{204}\text{Pb}$ (18.707); $^{207}\text{Pb}/^{204}\text{Pb}$ (15.607); $^{208}\text{Pb}/^{204}\text{Pb}$ (38.757); Pb = 25.3 ppm (sample Halt_088; Torsvik et al., 2015). We calculated the concentration of the starting melt with a 90:10 mix between a typical MORB (Pb = 0.185 ppm) and a typical OIB (Pb = 3.2 ppm) composition (Sun & McDonough, 1989) to be Pb = 0.59 ppm. As in Figure 4. Gray and pink fields respectively represent the Iceland IVID database (Harðardóttir et al., 2022) and Haltenbanken sediments (Torsvik et al., 2015).

with the main Icelandic array. Additionally, Vesteris samples partially overlap with some samples of Jan Mayen Island and Platform (Trønnes et al., 1999). In the Pb-Pb isotope spaces, Vesteris samples trend toward those of Tertiary lavas and mineralized alkaline complexes from NEGM north of Scoresby Sund (Jensen, 1998; Thirlwall et al., 1994). Örfafjökull, Tertiary mineralized alkaline complexes and lavas from NEGM and their underlying basement show the highest $\Delta 7/4$ values in the region, which were explained through the involvement of an enriched continental crust component (Jensen, 1998; Thirlwall et al., 1994; Torsvik et al., 2015).

The isotopic similarity in the Pb-Pb space suggests that an analogous enriched end-member (a crustal component) may be at play in the petrogenesis of Vesteris, in addition to the binary mixing between a depleted source (DM) and the main Iceland Plume (IP) (Figure 8).

For Örfafjökull, the positive $\Delta 7/4$ values have been assigned to the incorporation of continental crust from the Jan Mayen Microcontinent (JMCM) (Torsvik et al., 2015). Mixing models accounting for the isotopic Sr-Nd-Pb variability of Örfafjökull-Snæfell region requires the assimilation of 2%–6% continental crust to primitive basaltic melts. The presence of buried continental crust in SE Iceland is supported by its very thick crust as derived from gravity anomaly data and plate reconstructions suggesting that continental crust below Örfafjökull is a southward extension of the Jan Mayen microcontinent beneath southeast Iceland (Torsvik et al., 2015).

Another nearby example of contamination with continental crust is found at NEGM (Figure 1), where pyrites found in granite greisen vein, shale quartz vein, aplite, and granite from Werner Bjerger complex north from Scoresby Sund exhibit typical modern, crustal isotopic Pb ratios (Jensen, 1998; Stacey & Kramers, 1975; Zartman & Doe, 1981). For the Tertiary igneous rocks in the NEGM, positive $\Delta 7/4$ values have been explained by the assimilation of moderately radiogenic lead remobilized from local sedimentary basins and the basement (Jensen, 1998). Notably, the isotopic signatures of these rocks starkly differ from those of the Tertiary magmas exposed south of Scoresby Sund at the Kangerlussuaq igneous complex with remobilized Pb incorporated from low- μ Archean source (high-grade metamorphic Archean gneisses) (Jensen, 1998).

We propose that the entrainment of a crustal component as an enriched third end-member can explain the observed geochemical signatures of Vesteris rocks analyzed in this study (Figure 7). Because crustal lithologies are enriched in Sr, Nd, and Pb (ca. 325, 20, 12.6 ppm, respectively; Rudnick & Fountain, 1995) compared to depleted MORB mantle (DMM) (ca. 7.664, 0.581, 0.018 ppm; Workman & Hart, 2005), even minor contribution of a crustal component with high $^{87}\text{Sr}/^{86}\text{Sr}$, $^{207}\text{Pb}/^{204}\text{Pb}$ and $^{208}\text{Pb}/^{204}\text{Pb}$, intermediate $^{206}\text{Pb}/^{204}\text{Pb}$, and low $^{176}\text{Hf}/^{177}\text{Hf}$ and $^{143}\text{Nd}/^{144}\text{Nd}$ would dilute the signature of the original mantle-derived Vesteris composition.

We choose to model the continental crust contribution to the petrogenesis of Vesteris by binary mixing between the previously obtained regional mantle mixing and a crustal component with the isotopic signatures of the NEGM Tertiary basalts, igneous complexes, and sulfide occurrences north of the Scoresby Sund region (Jensen, 1998) due to their compositional similarities and geodynamic settings (Figure 1). We stress here that a simple mixing model does not provide a means to distinguish between pure bulk mixing at the source and partial melt assimilation en route to the surface. However, we specifically chose to model the contribution of this enriched end-member as a source component and not as an assimilant due to geodynamic reasons (see further discussion). As such, binary mixing is more suitable to the task than other assimilation models (e.g., Callegaro et al., 2013).

To reproduce Vesteris signatures, we start from a 90% DM-10% IP mixture along the DM-IP binary mixing line as previously established (see Section 5.2.2). This end-member is then mixed with a crustal component having high $^{207}\text{Pb}/^{204}\text{Pb}$ and $^{208}\text{Pb}/^{204}\text{Pb}$. The isotopic composition of the crust is here represented by the sulfides measured in Werner Bjerger alkaline complex from Malmbjerg (Jensen, 1998) (average of three samples; $^{206}\text{Pb}/^{204}\text{Pb}$ (18.722); $^{207}\text{Pb}/^{204}\text{Pb}$ (15.626); $^{208}\text{Pb}/^{204}\text{Pb}$ (38.919) (Table S2)). For the Pb concentration, we use 42 ppm, the average of 250 pre-Tertiary rocks from Gauss Halvø, Hudson Land, and Kuhn Ø as compiled by Jensen (1998). Notably, Jensen (1998) uses a similar model to reproduce the signature of Hold with Hope Tertiary basalts (Thirlwall et al., 1994). Our mixing model reproduces Vesteris Pb signatures by adding up to 1 wt% crust to the 90% DM-10% IP mantle source (Figure 8).

The addition of a crust-like contaminant as that of the NEGM margin, which is very enriched in Pb (42 ppm), reproduces Vesteris signatures better than if just adding an average upper crust (23 ppm) or an average lower crust (6 ppm) (Zartman & Haines, 1988). Using these latter Pb concentrations, we observe a decoupling between the effect produced by crust entrainment in the $^{207}\text{Pb}/^{204}\text{Pb}$ - $^{206}\text{Pb}/^{204}\text{Pb}$ space (1%–5%) and that produced in the $^{208}\text{Pb}/^{204}\text{Pb}$ - $^{206}\text{Pb}/^{204}\text{Pb}$ (2%–14%).

5.2.3.2. Crustal Assimilation

We note that an alternative mechanism to produce elevated $^{207}\text{Pb}/^{204}\text{Pb}$, $^{208}\text{Pb}/^{204}\text{Pb}$, and $^{87}\text{Sr}/^{86}\text{Sr}$ is assimilating oceanic sediments or altered oceanic crust (AOC).

In the Vesteris Seamount region, the crustal thickness derived from a *P*-wave velocity model based on sparse seismic data (Funck et al., 2014; Voss et al., 2009) indicates a crustal thickness of ca. 10 km, in agreement with gravity inversion data (C. Haase et al., 2017). Thick oceanic crust is explained by a higher spreading rate around chrons 18–20 in the Greenland basin than today (ca. 25 cm/yr, compared to 18 cm/yr for the last million years, i.e., Gaina, Nasuti, et al., 2017), and magmatic additions may have subsequently thickened this crust. Shallow assimilation of AOC during magma transport could occur during thermomechanical erosion of encompassing units. AOC assimilation during the magma transport to the surface cannot be ruled out (slight negative correlation of Pb isotopes (Figure S2 in Supporting Information S1) and U/Pb with MgO). It can be expected when OIB erupts over and ascends through thick oceanic crust. However, the alteration of the oceanic crust in the Atlantic Ocean is generally poorly constrained (Staudigel et al., 1996), and its assimilation is thus difficult to quantify.

Given the persistent seawater alteration of oceanic crust throughout millions of years, a hallmark characteristic of AOC is its high $^{87}\text{Sr}/^{86}\text{Sr}$ ratio (0.703636–0.707437; Staudigel et al., 1996). Another peculiarity of AOC melts is the high abundance of TiO_2 due to the melting of primary and secondary iron-titanium oxides and secondary titanite (e.g., Fisk et al., 1995). Vesteris has a higher $^{87}\text{Sr}/^{86}\text{Sr}$ for a given $^{143}\text{Nd}/^{144}\text{Nd}$ relative to NE Atlantic MORB and Iceland magmas. In addition, there is a very slight inverse correlation between $^{87}\text{Sr}/^{86}\text{Sr}$ and whole-rock MgO (Figure S2 in Supporting Information S1). This might result from the assimilation of AOC during differentiation in a magmatic lens. However, there is no marked positive Ti anomaly in Vesteris magmas (Figure 6). Assimilation of oceanic sediments is thus a more likely contaminant that could change (elevate) both $^{208}\text{Pb}/^{204}\text{Pb}$ and $^{207}\text{Pb}/^{204}\text{Pb}$ values. Because the feeding conduits of the seamount crossed both oceanic crust and Eocene sediments, and because the magnitude of such Ti anomaly would also depend on the proportion of AOC assimilation, a combination of the two processes is also possible.

Seafloor sediments are generally enriched in LREE, LILE (e.g., K), and Pb and exhibit enriched Sr-Nd-Hf isotope signatures and a negative Nb-Ta and Ti anomaly (Chauvel et al., 2008; Plank, 2014; Plank & Langmuir, 1998; Vervoort & Blichert-Toft, 1999; Vervoort et al., 2011). The intraplate setting of Vesteris Seamount in the Greenland Basin supports sediment assimilation as a viable mechanism, given that the old oceanic crust is overlaid by a thick sediment cover derived from the East Greenland shelf (mid-Miocene-present) with a total basin sediment volume of $1.37 \times 10^4 \text{ km}^3$ (Berger, 2006). Seismic reflectors at the seamount's base reveal a deeper base covered with ca. 1 km thick discontinuous sedimentary covers with uplifted and flexured layered sequences (Hempel et al., 1991). The only available sediment isotopic data in the literature are from the Norwegian basin—Haltenbanken sediments (Torsvik et al., 2015). As visible in Figure 7, they show a very broad range of isotopic signatures, encompassing the composition of the NEGM crust in $^{207}\text{Pb}/^{204}\text{Pb}$ – $^{206}\text{Pb}/^{204}\text{Pb}$ space but being generally lower in $^{208}\text{Pb}/^{204}\text{Pb}$ – $^{206}\text{Pb}/^{204}\text{Pb}$ space than the previously modeled crustal end member. We chose a sample from the Haltenbanken sediments compilation (Sample Halt_088; Torsvik et al., 2015) among those with elevated $^{207}\text{Pb}/^{204}\text{Pb}$ (15.607) and, more crucially, elevated $^{208}\text{Pb}/^{204}\text{Pb}$ (38.757), to represent the contaminant (Table S2). We calculated the concentration of the starting melt with a 90:10 mix between a typical MORB (Pb = 0.185 ppm) and a typical OIB (Pb = 3.2 ppm) composition (Sun & McDonough, 1989) to be Pb = 0.59 ppm. Mixing a melt of the previously calculated 90% DMM—10% IP or 85% DMM—15% IP source with up to 1% of this sediment is enough to raise the $^{207}\text{Pb}/^{204}\text{Pb}$ isotopic signatures to reach the ratios measured for Vesteris lavas. However, to reach Vesteris $^{208}\text{Pb}/^{204}\text{Pb}$, up to 8% of sediments need to be added. The same decoupling (more assimilation required in the $^{208}\text{Pb}/^{204}\text{Pb}$ vs. $^{206}\text{Pb}/^{204}\text{Pb}$ isotopic space) is observed if we model assimilation of this oceanic sediment by AFC (assimilation during fractional crystallization; De Paolo, 1981). Starting from a 90% DMM—10% IP-sourced parental melt, $^{207}\text{Pb}/^{204}\text{Pb}$ Vesteris compositions are reached after 10% crystallization, for a ratio of mass assimilation rate over mass fractionation rate (*r*) of 0.2 (for a bulk partition coefficient for Pb, *D* = 0.17). To reach the $^{208}\text{Pb}/^{204}\text{Pb}$ compositions, either the *r* parameter must reach 0.5 (unlikely high) or crystallization needs to proceed until 40% (unlikely for the basanites). Besides this decoupling in modeled results for $^{207}\text{Pb}/^{204}\text{Pb}$ and $^{208}\text{Pb}/^{204}\text{Pb}$ signatures, we also note that the isotopic signatures of our lavas are mostly spread in $^{206}\text{Pb}/^{204}\text{Pb}$ and thus do not align along an assimilation line. In addition, Vesteris rocks show a K negative anomaly, which would be likely reverted by significant assimilation of K-enriched sediments. We thus favor a model in which the enriched (crustal) component is entrained directly at the source, although minor amounts of sediment assimilation cannot be ruled out.

5.2.4. SCLM Component—Subcontinental Lithospheric Mantle

Several investigators have suggested that a regional Archean SCLM component might be prevalent in NE Atlantic, north of Jan Mayen (Northernmost Atlantic and Arctic) (e.g., Blichert-Toft et al., 2005; Goldstein et al., 2008). Unusually high ϵ_{Hf} signatures in MORB from Mohns and Knipovich ridges have hence been interpreted as reflecting a contribution of low-degree melts from old Greenland SCLM caught by upwelling asthenosphere beneath these ridges (K. M. Haase et al., 1996; Blichert-Toft et al., 2005). Greenlandic craton (3.6–3.7 Ga) has as well the lowest initial $^{207}\text{Pb}/^{204}\text{Pb}$ ratio and source U/Pb ratio ($\mu = 7.991$) found in all known cratons, attributed to lithosphere delamination, while source Th/U ratio is in range with other cratons (Luais & Hawkesworth, 2002). This is reflected as a relatively large proportion of an SCLM component in the mantle source of basalts from the Western Gakkel ridge owing to the negative $\Delta 7/4$ and high $\Delta 8/4$ signature of MORB (Goldstein et al., 2008). The presence of a SCLM component in the NE Atlantic and Arctic mantle is as well supported by $^{187}\text{Os}/^{188}\text{Os}$ ratios below 0.131 in a number of Icelandic flank zone basalts and in Jan Mayen basalts (Debaille et al., 2009) and below 0.126 in peridotite xenoliths from Pleistocene basalts in northern Spitsbergen (Choi et al., 2010). In NEGM lavas and dykes south of the Scoresby Sund (i.e., Kangerlussuaq, Tasiilap Karra dykes; Hanghøj et al., 1996; Holm, 1988; Jensen, 1998), significant involvement of SCLM relatively unradiogenic in $^{207}\text{Pb}/^{204}\text{Pb}$ and $^{206}\text{Pb}/^{204}\text{Pb}$ would limit the required amount of interaction with continental crust necessary to produce the enriched signatures.

In a diagram of ϵ_{Hf} versus ϵ_{Nd} , the positive ϵ_{Hf} values (12.98–13.58) shown by Vesteris samples (Figure 7b) plot above the mantle array and partially overlap a mixing hyperbola defined by MORB from the Mohns ridge and Jan Mayen platform (Blichert-Toft et al., 2005). The end-members of this hyperbola are interpreted by Blichert-Toft et al. (2005) as being the “C” component (Hanan & Graham, 1996) and a DMM, possibly contaminated by streaks of Greenlandic SCLM. This suggests that tectonically entrained SCLM caught in the asthenosphere, as indicated by the radiogenic ϵ_{Hf} isotope compositions of MORB present at these MOR segments, may also play a role in the Vesteris source. The ϵ_{Hf} signatures of Vesteris lavas and their decoupled Pb isotopic traits (negative $\Delta 7/4$ accompanied by positive $\Delta 8/4$) suggest that the SCLM domains may play a role in the source of this seamount, as they do elsewhere in the region. However, such an assumption cannot be properly quantified because of the general lack of Sr-Nd-Pb isotopic data on Greenlandic mantle xenoliths (especially north of Scoresby Sund). This means that a quantitative mixing model including an SCLM component would be presently highly speculative, especially because of the extreme trace element and Sr-Nd-Pb isotopic variability of this reservoir. Future measurements of $^{187}\text{Os}/^{188}\text{Os}$ ratios on Vesteris basalts and basanites would represent a strategic asset to test this hypothesis.

In summary, we can draw some information from the geochemical modeling of the Vesteris mantle source: (a) because Vesteris compositions differ even from those of the most enriched Icelandic lavas, the required enriched component cannot be “endemic” to the IP, but must be located elsewhere; (b) the SCLM has often been recognized in the region as a provider of enriched signatures, and we cannot exclude its contribution in the source of Vesteris lavas, as supported by their ϵ_{Hf} signatures and negative- $\Delta 7/4$ accompanied by high- $\Delta 8/4$. However, at present, it is impossible to constrain and quantify the contribution of SCLM as a source component of Vesteris because compositional data of SCLM north of Scoresby Sund are not available; (c) the most realistic contributor of Vesteris enriched signatures is a continental component, and it must be markedly enriched in Pb concentration; (d) The spread in $^{206}\text{Pb}/^{204}\text{Pb}$ ratios depicted by Vesteris samples is mostly controlled by the amount of main source mix (90%–85% DMM—10%–15% IP), while the proposed crustal component is responsible for raising Vesteris $^{208}\text{Pb}/^{204}\text{Pb}$ and $^{207}\text{Pb}/^{204}\text{Pb}$ signatures to higher values than the main Icelandic—N Atlantic MORB array; (e) we favor an entrainment of this crustal contaminant directly at the source.

5.3. Upper Mantle Structure and Lithospheric Control on Melting

In this section, we analyze the upper mantle structure as depicted by mantle tomographic models available for the study region and discuss possible implications for the mantle source mixing model (Figure 9). Tomographic models published in the last decade, which rely on a much-improved seismological database and modeling techniques, show that the IP has a complex structure, being possibly rooted at the core-mantle boundary and developing several conduits at shallower depths (1,200 km), perhaps nurturing several surface expressions (i.e., Iceland, Jan Mayen, and Svalbard; Rickers et al., 2013; Toyokuni et al., 2020). A more recent regional tomographic model based on waveform inversion of surface, *S*, and multiple *S* waves image the upper mantle, showing the complexity

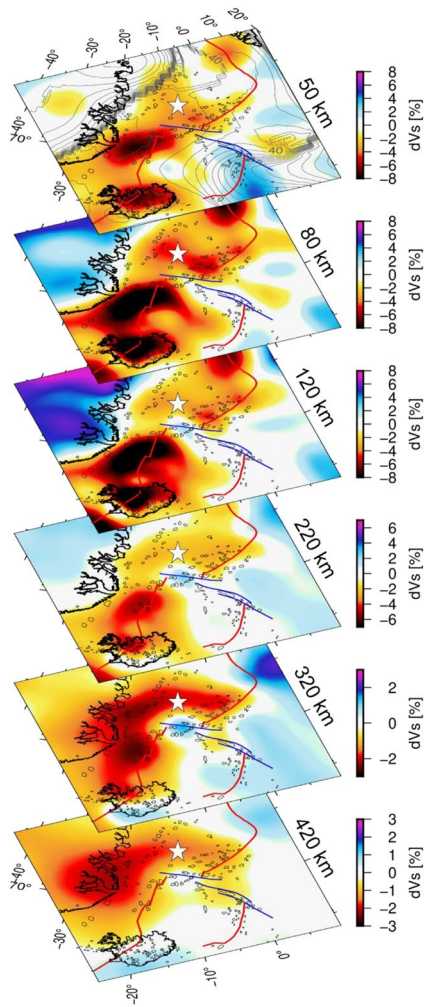


Figure 9. NAT2022 upper mantle tomographic model (Celli et al., 2021) as depth slices imaging S-wave velocity anomalies. These anomalies are shown in % from the reference seismic velocity at 50, 80, 120, 220, 320, and 420 km depth respectively. Lithospheric thickness contours on the 50 km depth slice are from the SL2013 model (Schaeffer & Lebedev, 2013). Red lines denote MOR, blue lines are fracture zones, and black contours outline the Gaina, Blischke, et al. (2017) seamounts; Vesteris Seamount is marked with a white star.

of the IP in greater detail than before (Celli et al., 2021). Assuming that the IP represents thermal upwelling, in this model, the IP conduit, centered under eastern Greenland at ca. 420 km, is branching and reaching under the Greenland Basin at 320 km and again at around 120–80 km (Figure 9). A shallower low-velocity anomaly becomes visible at 120 km below the Jan Mayen Platform, and then more prominent below VP at around 80 km. A deeper anomaly deflects eastward toward Mohn's ridge, avoiding the western JMFZ region, which appears to have an underlying colder asthenosphere (Figure 9). This colder region under the long-offset dual JMFZ may have acted as a physical barrier and reduced and deflected the upper mantle flow. Such deflections are also described at other hotspots (e.g., Canary/Cape Verde hotspot; Negrodo et al., 2022). The tomographic slice at 80 km (and probably also at 56 km, as shown by Celli et al. (2021)) indicates a NE-SW oriented negative anomaly that underlies the Vesteris Seamount and the group of seamounts SW of the Mohn's ridge. Its orientation may be slightly different from the one observed at 320 km, and we suggest this is due to the motion of the Greenland/North American plate relative to the mantle (i.e., Gaina, Nasuti, et al., 2017). The thicker lithosphere under the western Jan Mayen Fracture Zone may have also contributed to the shallower mantle flow deflection (Figure 9; panel showing a horizontal slice at 50 km; SL2013 model, Schaeffer & Lebedev, 2013). Considering the distribution of upper mantle anomalies detected by seismological data, we infer that a shallower reservoir (ca. 80–50 km) created by the IP may feed the Vesteris Seamount and possibly the seamount clusters in the western Greenland Basin.

The topography of the lithosphere-asthenosphere boundary and lithospheric thickness are also important parameters in estimating the location and cause of intraplate magmatic activity (Figure 10, Figure S5 in Supporting Information S1). Melt channeling through dykes and/or mantle upwelling is usually favored by abrupt lithospheric thickness changes (Figure 10). Mantle upwelling would follow lithospheric thinning from a thicker continental lithosphere toward a thinner continental margin (Boscaini et al., 2022; Conrad et al., 2010; Thompson & Gibson, 1991). We have evaluated several lithospheric models (gypsum (Simmons et al., 2010), s40rts (Ritsema et al., 2011), savani (Auer et al., 2014), semum2 (French et al., 2013), SL2013 (Schaeffer & Lebedev, 2013), mean (represent the mean of these five models) (Steinberger & Becker, 2018)) which show a range of lithospheric thickness beneath Vesteris from 35 km (SL2013sv) to 80 km (gypsum and s40rts) (Figure 10, Figure S5 in Supporting Information S1). The mean model and semum2 and savani models show a lithospheric thickness of roughly 50 km (Figure 10 and Figure S5 in Supporting Information S1). The inverse lithospheric topography

inferred from the SL2013 model (Schaeffer & Lebedev, 2013) images well-pronounced lithospheric steps at East Greenland and Norway margins. In numerical fluid dynamic experiments reproducing plume/ridge interaction, the slope of the base of the oceanic lithosphere is a crucial factor in driving the plume flow (Kincaid et al., 1995). The steeper the gradient is, the more likely plume material will flow. This suggests that lateral asthenospheric flow traveling from the margin of Greenland (Figure 9) toward Mohn's Ridge would rapidly rise and decompress beneath the upwardly sloping region of the lithosphere (Figure 10 and Figure S5 in Supporting Information S1). Melting could hence be triggered underneath Vesteris because the lateral asthenospheric flow encounters rapid gradients in the thickness of the lithosphere of 250 km at the Greenland cratonic root to 35–80 km in the Greenland Basin, depending on a model (Steinberger & Becker, 2018) (Figure 10).

5.4. Melting Model for Vesteris Seamount Rocks

The major element composition of the most primitive Vesteris rocks (alkali basalt/basanites) overlaps or falls near that of experimental melts derived from silica-undersaturated pyroxenite melting at 2 GPa (MIX1G, Hirschmann

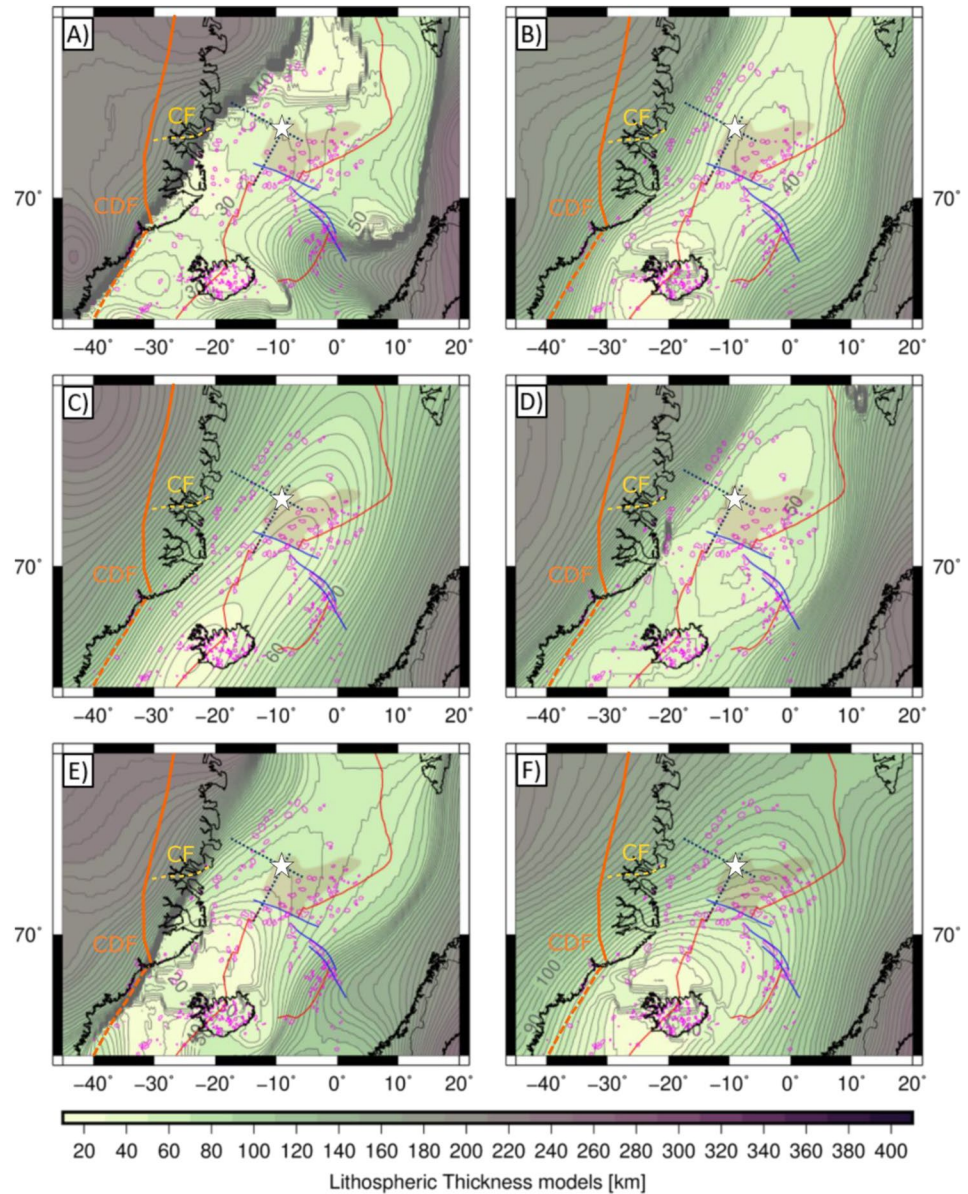


Figure 10. Lithospheric thickness maps produced from different tomography models as summarized by Steinberger and Becker (2018): (a) SL2013 (Schaeffer & Lebedev, 2013), (b) s40rts (Ritsema et al., 2011), (c) mean of 5 presented models (Steinberger & Becker, 2018), (d) savani (Auer et al., 2014), (e) semum2 (French et al., 2013), (f) gypsum (Simmons et al., 2010). Vesteris Plateau, a region ($\sim 1.12 \times 10^5 \text{ km}^2$) of uplifted oceanic seafloor (Zhang et al., 2020), is represented by pale pink shading. The dotted black line represents a track where the lithospheric depths of all models are extracted (Figure S5 in Supporting Information S1). Thin magenta contours outline Gaina, Blischke, et al. (2017) seamounts; Vesteris Seamount is marked with a white star. The orange line represents the Caledonian Deformation Front (CDF) (Gee et al., 2008), and the yellow line is the Central Fjord (CF), where an east-dipping high-velocity oceanic slab was documented by Schiffer et al. (2014, 2016, 2020).

et al., 2003), as shown in Figure 6. This observation is generally backed up by forward numerical models of dynamic melting performed with REEBOX PRO (Brown & Leshner, 2016) (Table S3). The best match with the trace element compositions of our Vesteris basanites and alkali basalt is obtained by active melting a mixed lithology (50% peridotite—50% pyroxenite) source under a pre-existing lithosphere of 65 km (Figure 6 and Figure S5 in Supporting Information S1). The maximum extent of melting (F_{max}) for this mixed source at the top of the columnar regime (65 km depth, 1.99 GPa pressure) is estimated to be 1% for the peridotite and 2% for the pyroxenite. The anhydrous peridotite (pyrolite) has a primitive mantle trace element composition (McDonough &

Sun, 1995), while the Si-undersaturated pyroxenite (MIX1G) has an N-MORB trace element composition (Sun & McDonough, 1989). Pooled melts aggregated over this rather short columnar melting regime (i.e., $P_i = 2.31$ GPa; $P_f = 1.99$ GPa) are dominated by a greater proportion of pyroxenite-melts (59%) relative to peridotite-melts (41%). Modeled melts of either pure MIX1G or pure pyrolite under a range of plausible mantle potential temperature (T_p) and pre-existing lithospheric thicknesses fail to reproduce the trace element composition of our Vesteris data set. The pyroxenitic lithology could be produced by reacting the lithospheric (crustal or SCLM) domains delaminated from Greenland with the ambient peridotite (e.g., Yaxley & Green, 1998). The interactions between siliceous partial melts of eclogitic and peridotite might have formed pyroxenitic veins (Yaxley & Green, 1998). Alternatively, the material thermally eroded from the Greenland keel could have already been pyroxenitic (Hirschmann et al., 2003). We conclude that the melting model and resulting depth and temperature results agree with the geodynamic setting of the Vesteris seamount and our geochemical results.

The numerical REEBOX simulation indicates that the ambient mantle (pyrolite) source composition underneath Vesteris might be primitive rather than similar to that of the DM. First, this outcome is inconsistent with the end-member proportions (90%–85% DMM—10%–15% IP) estimated by the previous isotopic modeling. One way to resolve this paradox would be to involve a fourth component, unradiogenic in $^{206}\text{Pb}/^{204}\text{Pb}$, such as the Archean Greenlandic SCLM. Such an addition would require a higher proportion of IP in order to match the moderately radiogenic $^{206}\text{Pb}/^{204}\text{Pb}$ of Vesteris. It also indicates that the potential temperature (1,330°C) at the time of volcanism at Vesteris might not have been warmer than the ambient mantle temperature (1,300–1,400°C, Herzberg & Gazel, 2009). However, the estimated final depth of melting falls in the depth range (80–50 km) where a low seismic wave mantle anomaly is presently detected underneath Vesteris (Figure 9). This anomaly might be a secondary branch of the Icelandic plume or an enriched mantle blob released by the Icelandic plume. The remoteness of this anomaly, up to 1,000 km relative to the main Icelandic conduct, would have favored heat loss of the Icelandic material during transport, lowering its temperature underneath Vesteris relative to that of the main Icelandic conduit. Such a thermal dissipation mechanism is well known for plume material spreading over long distances (Ribe & Christensen, 1999).

5.5. Potential Mechanisms and Location of Contamination/Mixing: Entrainment of Continental Crust and SCLM

Based on our geochemical results, the described mantle tomography model of the NE Atlantic, the lithospheric thickness models (Figures 9 and 10 and Figure S5 in Supporting Information S1), and the forward melting model produced (REEBOX PRO model; Brown & Leshner, 2016), we propose the following geodynamic scenario to explain the origin of Vesteris seamount. Tomographic models (Rickers et al., 2013 and, more recently, Celli et al., 2021) image a mantle anomaly between 400 and 320 km that deviates from Iceland's plume and flows northward under the East Greenland margin and Greenland Basin. Horizontal slices of *S*-wave velocity anomalies show eastward deflection of the flow just north of the western JMFZ (Figure 9). Several studies show that the East Greenland margin (Scoresby Sund and Fjordland region), thinned due to continental rifting, has heat flow values higher (>100 mW/m²) than expected at a passive margin (Artemieva, 2019). The presence of a northward deflection of the IP could also explain such a characteristic.

We note that the steep gradient of lithospheric thickness, from about 250 km of Greenland cratonic root (Steinberger & Becker, 2018) to around 50 km in the Greenland Basin, would enhance the decompression melting of such a rising mantle and channel it upwards along a steep slope between thick continental and thinner oceanic lithosphere. Therefore, Vesteris Seamount is possibly nurtured by a plume branch that is eroding the Greenland lithosphere and may detach enriched blobs or veins of SCLM (Blichert-Toft et al., 2005; Elkins et al., 2014) and possibly crustal streaks (Rankenburg et al., 2005) and transport them through the ambient mantle below the Greenland Basin (Figure 11). Both SCLM and continental crust are geochemically enriched and have been previously advocated as local contributors to the magmatism in the region (e.g., Blichert-Toft et al., 2005; Jensen, 1998; Torsvik et al., 2015; Trønnes et al., 1999). Archean SCLM is found beneath the Greenland craton, ~500 km west of Vesteris Seamount, and might be eroded by the Icelandic plume flow during its ascent. In addition, an upper mantle structure in East Greenland was interpreted as a fossil Caledonian subduction complex based on teleseismic receiver function analyses (Schiffer et al., 2014, 2016, 2020). A suture resulting from an east-dipping subduction zone (high-velocity layer (V_p N 8.3 km/s)) is entrained in the lithosphere of the Central Fjord region, as marked in Figure 10. Petrological and geophysical models show sub-crustal structure in the lower crust/uppermost mantle as a combination of eclogitized mafic crust or older igneous intrusions overlaid with mafic intrusions, and serpentinized peridotite (Schiffer et al., 2016). Such a slab remnant could bring a variable

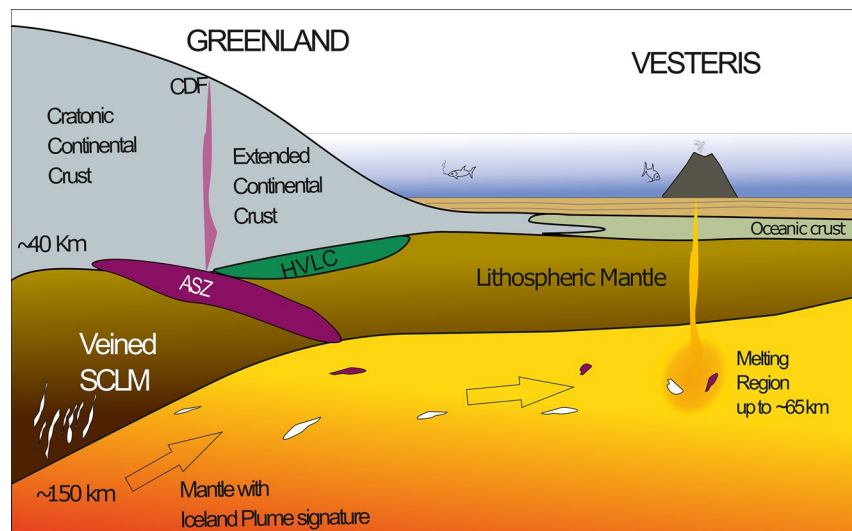


Figure 11. A simplified conceptual model for the formation of Vesteris Seamount, along a profile trending west—north-east from NE Greenland to Vesteris. The upper mantle was influenced by the northward flowing Iceland plume branch that may have eroded the Greenland and entrain continental crust and sub-continental lithospheric mantle geochemical signature in the Vesteris Seamount melting region. A fossil Caledonian subduction complex—Ancient subduction zone (ASZ) and high-velocity lower crust (HVLC) in East Greenland are based on Schiffer et al. (2014, 2016, 2020). The pink field represents the Caledonian Deformation Front (CDF) (Gee et al., 2008).

amount of Archean, Proterozoic, and Paleozoic basement domains deeper into the crust or uppermost mantle that could contaminate and enrich the source of Vesteris lavas (Figure 11).

It is observed elsewhere that SCLM delaminated material could be brought by plume thermal erosion in the surrounding convecting asthenosphere (e.g., Class & le Roex, 2006; Meyzen et al., 2007). Even though the mechanisms by which such material is detached and transported to ocean basins have not been well constrained, its contribution has been proposed to account for the peculiar Sr-Nd-Pb-Hf isotopic signatures of South-Atlantic MORB (African craton) (Meyzen et al., 2007) and Walvis Ridge (Congo and Rio Apa—Luis Alves cratons) (Class & le Roex, 2006). Therefore, carving the East Greenland margin by the IP branch is a feasible mechanism to explain the sampling of various cratonic and passive margin structures (allowing both SCLM and continental crust mixing/assimilation) by sources that produced Vesteris magmatism.

Our geochemical results and conceptual model show for the first time that the northward continuation of the IP impacted the solitary Vesteris seamount formation. This contrasts the published models that invoke a purely uppermost mantle, rifting-related source, and mechanisms for its formation. Given that the seamount may have been formed by multiple volcanic events (Mertz & Renne, 1995; Moreno et al., 2021), we cannot completely discard that more recent tectonic events contributed to the construction of part of its edifice. Vesteris seamount is remotely located relative to active plate boundaries, and the known direction of motion for Greenland/North America relative to the mantle (Figure 5 in Gaina, Nasuti, et al., 2017) cannot explain the volcanic edifice shape. Proper lithospheric stress and paleo-stress modeling are beyond the scope of this study, but it could shed more light on the origin and tectono-magmatic evolution of this enigmatic seamount.

6. Conclusions

Major and trace elements and high-precision Sr-Nd-Pb-Hf isotopes from lavas dredged from the Vesteris Seamount are presented in this study, and the results allow us to trace the mantle source characteristics and a plausible geodynamic mechanism for the origin of this seamount. Published mantle tomography and lithospheric models helped to understand the lithosphere and upper mantle structure in the Vesteris Seamount region. This integrated geochemical and geophysical study provided a more comprehensive and contextualized understanding of the processes that led to the formation of Vesteris Seamount. Our main conclusions are summarized as follows:

- Deep mantle low-velocity anomalies, possibly connected to the IP, contributed to forming the Vesteris Seamount volcanic construction. This supports previous hypotheses suggesting that the IP has played a

significant role in shaping the geology of this region (active melting scenarios) and is in contrast to prior studies that invoke purely local tectonics and uppermost mantle sources (passive melting scenarios) for this volcanic edifice.

- Compared with the dominant signatures displayed by MORB and Iceland volcanism in the region, Vesteris has anomalous isotopic compositions that cannot be explained solely by the complementary contributions of the DM and the Icelandic plume. We suggest that the additional enriched component able to produce Vesteris high-radiogenic $^{207}\text{Pb}/^{204}\text{Pb}$ and $^{208}\text{Pb}/^{204}\text{Pb}$ signatures is of continental origin. Our favored scenario envisages a remobilized crustal component from the East Greenland basement, contributing directly to the source. Alternatively, the assimilation of oceanic sediments or locally AOC could explain the observed signatures, although we flag it as less likely based on geochemical evidence.
- The involvement of Archean SCLM in the source of Vesteris is likely because this component is widespread in the region (e.g., Mohns MORB) and supported by the ϵ_{Hf} composition of Vesteris lavas and their low $\Delta 7/4$ accompanied by high $\Delta 8/4$. However, we cannot quantitatively constrain its contribution due to the lack of available isotopic data for the NE Greenland SCLM.
- The following source petrogenetic scenario for Vesteris is proposed by merging geochemical and geophysical observations: A northward deflected branch of the main IP branch beneath East Greenland produced delamination of lithospheric domains from the Greenland craton and margin. It reached the Greenland basin area beneath the Vesteris seamount using the steep gradient of lithospheric thickness. Here, a mixture of plume-derived sources, ambient depleted asthenosphere, and enriched lithospheric material (pyroxenitic) could melt up to a maximum 65 km depth to produce the alkaline, isotopically enriched magmas that formed Vesteris.

We note that this study has some limitations. The lack of high-resolution seismic data and comprehensive isotopic data coverage has prevented a complete understanding of the subsurface plumbing system of Vesteris Seamount and the influence of the IP. In particular, the entrainment mechanism of the enriched component cannot be completely resolved at this stage. Similarly, the absence of regional petrological data sets prevented a quantitative evaluation of the SCLM contribution. Further research, including more detailed constraints on the Vesteris magmas evolution (fractionation trends, magma chamber processes, open-vs. closed-system differentiation), is needed to address these limitations and provide a complete picture of the processes shaping this dynamic region.

Data Availability Statement

All data supporting the findings of this study are available within the supplementary material and the data files are archived at Belosa (2023).

Acknowledgments

We are grateful to Reidar Trønnes for providing the standards for geochemical analyses and extensive discussions about Vesteris and the geochemical provincialism of NE Atlantic. We thank the Volcanic Basin Petroleum Research (VBPR) and TGS Norway for organizing the survey and kindly providing the samples. We thank Wolfgang Bach, Karsten Haase, and Cristoph Beier for their collaboration and for providing multibeam bathymetry data for Vesteris Seamount. We are grateful to Christian Tegner, whose thorough reviews have greatly improved our manuscript. We acknowledge financial support from the Research Council of Norway (NFR) through its Centers of Excellence scheme, project number 223272 (CEED) and project number 332523 (PHAB). LB and CG acknowledge support from NFR through project NORRAM 309477. S.C. acknowledges funding from the NFR Young Research Talent Grant 301096. A.M. acknowledges NFR support through the HOTMUD project number 288299.

References

- Abouchami, W., Galer, S. J. G., & Hofmann, A. W. (2000). High precision lead isotope systematics of lavas from the Hawaiian Scientific Drilling Project. *Chemical Geology*, 169(1), 187–209. [https://doi.org/10.1016/S0009-2541\(00\)00328-4](https://doi.org/10.1016/S0009-2541(00)00328-4)
- Alt, J. C. (1995). Subseafloor processes in Mid-Ocean Ridge hydrothermal systems. In *Seafloor hydrothermal systems: Physical, chemical, biological, and geological interactions* (pp. 85–114). American Geophysical Union (AGU). <https://doi.org/10.1029/GM091p0085>
- Artemieva, I. M. (2019). Lithosphere thermal thickness and geothermal heat flux in Greenland from a new thermal isostasy method. *Earth-Science Reviews*, 188, 469–481. <https://doi.org/10.1016/j.earscirev.2018.10.015>
- Auer, L., Boschi, L., Becker, T. W., Nissen-Meyer, T., & Giardini, D. (2014). Savani: A variable resolution whole-mantle model of anisotropic shear velocity variations based on multiple data sets. *Journal of Geophysical Research: Solid Earth*, 119(4), 3006–3034. <https://doi.org/10.1002/2013JB010773>
- Ballmer, M. D., van Hunen, J., Ito, G., Bianco, T. A., & Tackley, P. J. (2009). Intraplate volcanism with complex age-distance patterns: A case for small-scale sublithospheric convection. *Geochemistry, Geophysics, Geosystems*, 10(6), Q06015. <https://doi.org/10.1029/2009GC002386>
- Batiza, R. (1982). Abundances, distribution, and sizes of volcanoes in the Pacific Ocean and implications for the origin of non-hotspot volcanoes. *Earth and Planetary Science Letters*, 60(2), 195–206. [https://doi.org/10.1016/0012-821x\(82\)90003-6](https://doi.org/10.1016/0012-821x(82)90003-6)
- Béguelin, P., Bizimis, M., Beier, C., & Turner, S. (2017). Rift–plume interaction reveals multiple generations of recycled oceanic crust in Azores lavas. *Geochimica et Cosmochimica Acta*, 218, 132–152. <https://doi.org/10.1016/j.gca.2017.09.015>
- Belosa, L. (2023). Deep mantle component and continental crust remobilization in the source of Vesteris Seamount, East Greenland margin [Dataset]. *Geochemistry, Geophysics, Geosystems*. Zenodo. <https://doi.org/10.5281/zenodo.10405490>
- Berger, G. W. (2006). Trans-arctic-ocean tests of fine-silt luminescence sediment dating provide a basis for an additional geochronometer for this region. *Quaternary Science Reviews*, 25(19), 2529–2551. <https://doi.org/10.1016/j.quascirev.2005.07.024>
- Bernstein, S., Leslie, A. G., Higgins, A. K., & Brooks, C. K. (2000). Tertiary alkaline volcanics in the Nunatak region, northeast Greenland: New observations and comparison with Siberian maymechites. *Lithos*, 53(1), 1–20. [https://doi.org/10.1016/S0024-4937\(00\)00012-8](https://doi.org/10.1016/S0024-4937(00)00012-8)
- Blichert-Toft, J., Agraniér, A., Andres, M., Kingsley, R., Schilling, J.-G., & Albarède, F. (2005). Geochemical segmentation of the Mid-Atlantic Ridge north of Iceland and ridge–hot spot interaction in the North Atlantic. *Geochemistry, Geophysics, Geosystems*, 6(1), Q06010. <https://doi.org/10.1029/2004GC000788>

- Boscaini, A., Marzoli, A., Bertrand, H., Chiaradia, M., Jourdan, F., Faccenda, M., et al. (2022). Cratonic keels controlled the emplacement of the central Atlantic magmatic province (CAMP). *Earth and Planetary Science Letters*, 584, 117480. <https://doi.org/10.1016/j.epsl.2022.117480>
- Boyd, F. R., & Mertzman, S. A. (1987). Composition and structure of the Kaapvaal lithosphere, southern Africa (Vol. 12).
- Brown, E. L., & Leshner, C. E. (2016). REEBOX PRO: A forward model simulating melting of thermally and lithologically variable upwelling mantle. *Geochemistry, Geophysics, Geosystems*, 17(10), 3929–3968. <https://doi.org/10.1002/2016GC006579>
- Buck, W. R., & Parmentier, E. M. (1986). Convection beneath young oceanic lithosphere: Implications for thermal structure and gravity. *Journal of Geophysical Research*, 91(B2), 1961–1974. <https://doi.org/10.1029/JB0911B02p01961>
- Callegaro, S., Marzoli, A., Bertrand, H., Chiaradia, M., Reisberg, L., Meyzen, C., et al. (2013). Upper and lower crust recycling in the source of CAMP basaltic dykes from southeastern North America. *Earth and Planetary Science Letters*, 376, 186–199. <https://doi.org/10.1016/j.epsl.2013.06.023>
- Celli, N. L., Lebedev, S., Schaeffer, A. J., & Gaina, C. (2021). The tilted Iceland Plume and its effect on the North Atlantic evolution and magmatism. *Earth and Planetary Science Letters*, 569, 117048. <https://doi.org/10.1016/j.epsl.2021.117048>
- Chauvel, C., Lewin, E., Carpentier, M., Arndt, N. T., & Marini, J.-C. (2008). Role of recycled oceanic basalt and sediment in generating the Hf–Nd mantle array. *Nature Geoscience*, 1(1), 64–67. <https://doi.org/10.1038/ngeo.2007.51>
- Chazot, G., Menzies, M. A., & Harte, B. (1996). Determination of partition coefficients between apatite, clinopyroxene, amphibole, and melt in natural spinel lherzolites from Yemen: Implications for wet melting of the lithospheric mantle. *Geochimica et Cosmochimica Acta*, 60(3), 423–437. [https://doi.org/10.1016/0016-7037\(95\)00412-2](https://doi.org/10.1016/0016-7037(95)00412-2)
- Chekol, T., Kobayashi, K., Yokoyama, T., Sakaguchi, C., & Nakamura, E. (2011). Timescales of magma differentiation from basalt to andesite beneath Hekla Volcano, Iceland: Constraints from U-series disequilibria in lavas from the last quarter-millennium flows. *Geochimica et Cosmochimica Acta*, 75(1), 256–283. <https://doi.org/10.1016/j.gca.2010.10.001>
- Cherkis, N. Z., Steinmetz, S., Schreiber, R., Thiede, J., & Theiner, J. (1994). Vesteris seamount: An enigma in the Greenland basin. *Marine Geophysical Researches*, 16(4), 287–301. <https://doi.org/10.1007/bf01224746>
- Chernysheva, E. A., & Kharin, G. S. (2007). Alkaline volcanism in the history of the Norwegian-Greenland basin. *Petrology*, 15(3), 296–301. <https://doi.org/10.1134/S086959110703006X>
- Choi, S. H., Suzuki, K., Mukasa, S. B., Lee, J.-I., & Jung, H. (2010). Lu–Hf and Re–Os systematics of peridotite xenoliths from Spitsbergen, western Svalbard: Implications for mantle–crust coupling. *Earth and Planetary Science Letters*, 297(1), 121–132. <https://doi.org/10.1016/j.epsl.2010.06.013>
- Class, C., & le Roex, A. P. (2006). Continental material in the shallow oceanic mantle—How does it get there? *Geology*, 34(3), 129–132. <https://doi.org/10.1130/G21943.1>
- Conrad, C. P., Bianco, T. A., Smith, E. I., & Wessel, P. (2010). Asthenospheric shear controls global patterns of intraplate volcanism. 2010, U51A-0027.
- Cooper, L. B., Bachmann, O., & Huber, C. (2015). Volatile budget of Tenerife phonolites inferred from textural zonation of S-rich hauyne. *Geology*, 43(5), 423–426. <https://doi.org/10.1130/G36505.1>
- Dasgupta, R., Jackson, M. G., & Lee, C.-T. A. (2010). Major element chemistry of ocean island basalts—Conditions of mantle melting and heterogeneity of mantle source. *Earth and Planetary Science Letters*, 289(3), 377–392. <https://doi.org/10.1016/j.epsl.2009.11.027>
- Debaille, V., Trønnes, R. G., Brandon, A. D., Waight, T. E., Graham, D. W., & Lee, C.-T. A. (2009). Primitive off-rift basalts from Iceland and Jan Mayen: Os–Isotopic evidence for a mantle source containing enriched subcontinental lithosphere. *Geochimica et Cosmochimica Acta*, 73(11), 3423–3449. <https://doi.org/10.1016/j.gca.2009.03.002>
- DePaolo, D. J. (1981). Trace element and isotopic effects of combined wallrock assimilation and fractional crystallization. *Earth and Planetary Science Letters*, 53(2), 189–202. [https://doi.org/10.1016/0012-821x\(81\)90153-9](https://doi.org/10.1016/0012-821x(81)90153-9)
- DePaolo, D. J., & Wasserburg, G. J. (1979). Sm–Nd age of the Stillwater complex and the mantle evolution curve for neodymium. *Geochimica et Cosmochimica Acta*, 43(7), 999–1008. [https://doi.org/10.1016/0016-7037\(79\)90089-9](https://doi.org/10.1016/0016-7037(79)90089-9)
- Dickin, A. P. (2018). *Radiogenic isotope geology*. Cambridge University Press.
- Donnelly, T., Francheteau, J., Bryan, W., Robinson, P., Flower, M., Salisbury, M., et al. (1980). *Initial reports of the deep sea drilling project, 51/52/53* (Vol. 51–53). U.S. Government Printing Office. <https://doi.org/10.2973/dsdp.proc.515253.1980>
- Ehrlich, S., Gavrieli, I., Dor, L.-B., & Halicz, L. (2001). Direct high-precision measurements of the ⁸⁷Sr/⁸⁶Sr isotope ratio in natural water, carbonates and related materials by multiple collector inductively coupled plasma mass spectrometry (MC-ICP-MS). *Journal of Analytical Atomic Spectrometry*, 16(12), 1389–1392. <https://doi.org/10.1039/B107996B>
- Elkins, L. J., Hamelin, C., Blichert-Toft, J., Scott, S. R., Sims, K. W. W., Yeo, I. A., et al. (2016). North Atlantic hotspot–ridge interaction near Jan Mayen Island. *Geochemical Perspectives Letters*, 2(1), 55–67. <https://doi.org/10.7185/geochemlet.1606>
- Elkins, L. J., Sims, K. W. W., Prytulak, J., Blichert-Toft, J., Elliott, T., Blusztajn, J., et al. (2014). Melt generation beneath Arctic Ridges: Implications from U decay series disequilibria in the Mohns, Knipovich, and Gakkel Ridges. *Geochimica et Cosmochimica Acta*, 127, 140–170. <https://doi.org/10.1016/j.gca.2013.11.031>
- Elliott, T. R., Hawkesworth, C. J., & Grönvold, K. (1991). Dynamic melting of the Iceland plume. *Nature*, 351(6323), 201–206. <https://doi.org/10.1038/351201a0>
- Fisk, M. R., Johnson, K. T. M., & Alt, J. C. (1995). Effect of assimilation of altered oceanic crust on magma chemistry: An experimental study. *Effect of Assimilation of Altered Oceanic Crust on Magma Chemistry: An Experimental Study*, 137–40, 43–51.
- Fitton, J. G., Saunders, A. D., Kempton, P. D., & Hardarson, B. S. (2003). Does depleted mantle form an intrinsic part of the Iceland plume? *Geochemistry, Geophysics, Geosystems*, 4(3), 1032. <https://doi.org/10.1029/2002GC000424>
- Fitton, J. G., Saunders, A. D., Norry, M. J., Hardarson, B. S., & Taylor, R. N. (1997). Thermal and chemical structure of the Iceland plume. *Earth and Planetary Science Letters*, 153(3), 197–208. [https://doi.org/10.1016/S0012-821X\(97\)00170-2](https://doi.org/10.1016/S0012-821X(97)00170-2)
- Forsyth, D., Harmon, N., Scheirer, D., & Duncan, R. (2006). Distribution of recent volcanism and the morphology of seamounts and ridges in the GLIMPSE study area: Implications for the lithospheric cracking hypothesis for the origin of intraplate, non-hot spot volcanic chains. *Journal of Geophysical Research*, 111(B11), B03202. <https://doi.org/10.1029/2005JB004075>
- French, S., Lekic, V., & Romanowicz, B. (2013). Waveform tomography reveals channeled flow at the base of the oceanic asthenosphere. *Science*, 342(6155), 227–230. <https://doi.org/10.1126/science.1241514>
- Frisby, C., Bizimis, M., & Mallick, S. (2016). Hf–Nd isotope decoupling in bulk abyssal peridotites due to serpentinization. *Chemical Geology*, 440, 60–72. <https://doi.org/10.1016/j.chemgeo.2016.07.006>
- Funck, T., Hopper, J., Fattah, R., Blischke, A., Ebbing, J., Erlendsson, O., et al. (2014). Crustal structure. In J. R. Hopper & M. S. Stoker (Eds.), *Geological survey of Denmark and Greenland* (pp. 69–126). Retrieved from <http://www.nagtec.org/home/seam>

- Gaina, C., Blischke, A., Geissler, W. H., Kimbell, G. S., & Erlendsson, Ö. (2017). Seamounts and oceanic igneous features in the NE Atlantic: A link between plate motions and mantle dynamics. *Geological Society, London, Special Publications*, 447(1), 419–442. <https://doi.org/10.1144/sp447.6>
- Gaina, C., Gernigon, L., & Ball, P. (2009). Palaeocene–Recent plate boundaries in the NE Atlantic and the formation of the Jan Mayen microcontinent. *Journal of the Geological Society*, 166(4), 601–616. <https://doi.org/10.1144/0016-76492008-112>
- Gaina, C., Nasuti, A., Kimbell, G. S., & Blischke, A. (2017). Break-up and seafloor spreading domains in the NE Atlantic. *Geological Society, London, Special Publications*, 447(1), 393–417. <https://doi.org/10.1144/sp447.12>
- GEBCO Bathymetric Compilation Group 2021. (2021). *The GEBCO_2021 Grid—A continuous terrain model of the global oceans and land. (Version 1) [Documents, Network common data form]*. NERC EDS British Oceanographic Data Centre NOC. <https://doi.org/10.5285/C6612CBE-50B3-0CFF-E053-6C86ABC09F8F>
- Gee, D. G., Fossen, H., Henriksen, N., & Higgins, A. K. (2008). From the early Paleozoic platforms of Baltica and Laurentia to the Caledonide Orogen of Scandinavia and Greenland. *Episodes Journal of International Geoscience*, 31(1), 44–51. <https://doi.org/10.18814/epiugs/2008/v31i1/007>
- Gernigon, L., Gaina, C., Olesen, O., Ball, P. J., Péron-Pinvidic, G., & Yamasaki, T. (2012). The Norway Basin revisited: From continental breakup to spreading ridge extinction. *Marine and Petroleum Geology*, 35(1), 1–19. <https://doi.org/10.1016/j.marpetgeo.2012.02.015>
- Goldstein, S. L., Soffer, G., Langmuir, C. H., Lehnert, K. A., Graham, D. W., & Michael, P. J. (2008). Origin of a ‘Southern Hemisphere’ geochemical signature in the Arctic upper mantle. *Nature*, 453(7191), 89–93. <https://doi.org/10.1038/nature06919>
- Grønlie, G., Chapman, M., & Talwani, M. (1979). Mayen Ridge and Iceland plateau: Origin and evolution.
- Haase, C., Ebbing, J., & Funck, T. (2017). A 3D regional crustal model of the NE Atlantic based on seismic and gravity data. *Geological Society, London, Special Publications*, 447(1), 233–247. <https://doi.org/10.1144/sp447.8>
- Haase, K. M., & Devey, C. W. (1994). The petrology and geochemistry of Vesteris seamount, Greenland basin—An intraplate alkaline volcano of non-plume origin. *Journal of Petrology*, 35(2), 295–328. <https://doi.org/10.1093/petrology/35.2.295>
- Haase, K. M., Devey, C. W., Mertz, D. F., Stoffers, P., & Garbe-Schönberg, D. (1996). Geochemistry of lavas from Mohns Ridge, Norwegian-Greenland sea: Implications for melting conditions and magma sources near Jan Mayen. *Contributions to Mineralogy and Petrology*, 123(3), 223–237. <https://doi.org/10.1007/s004100050152>
- Hanan, B. B., & Graham, D. W. (1996). Lead and Helium isotope evidence from oceanic basalts for a common deep source of mantle plumes. *Science*, 272(5264), 991–995. <https://doi.org/10.1126/science.272.5264.991>
- Hanghøj, K., Storey, M., & Stecher, O. (1996). An isotope study of the East Greenland tertiary dyke Swarm: Evidence for an old lithospheric mantle source in the North Atlantic. *Eos, Transactions American Geophysical Union*, 77, 844.
- Hards, V. L., Kempton, P. D., & Thompson, R. N. (1995). The heterogeneous Iceland plume: New insights from the alkaline basalts of the Snaefell volcanic centre. *Journal of the Geological Society*, 152(6), 1003–1009. <https://doi.org/10.1144/GSL.JGS.1995.152.01.21>
- Hart, S. R. (1984). A large-scale isotope anomaly in the Southern Hemisphere mantle. *Nature*, 309(5971), 753–757. <https://doi.org/10.1038/309753a0>
- Harðardóttir, S., Matthews, S., Halldórsson, S. A., & Jackson, M. G. (2022). Spatial distribution and geochemical characterization of Icelandic mantle end-members: Implications for plume geometry and melting processes. *Chemical Geology*, 604, 120930. <https://doi.org/10.1016/j.chemgeo.2022.120930>
- Haxby, W. F., & Weissel, J. K. (1986). Evidence for small-scale mantle convection from Seasat altimeter data. *Journal of Geophysical Research*, 91(B3), 3507–3520. <https://doi.org/10.1029/JB091iB03p03507>
- Hemond, C., Arndt, N. T., Lichtenstein, U., Hofmann, A. W., Oskarsson, N., & Steinthorsson, S. (1993). The heterogeneous Iceland plume: Nd–Sr–O isotopes and trace element constraints. *Journal of Geophysical Research*, 98(B9), 15833–15850. <https://doi.org/10.1029/93JB01093>
- Hempel, P., Schreiber, R., Johnson, L., & Thiede, J. (1991). The Vesterisbanken Seamount (Greenland Basin): Patterns of morphology and sediment distribution. *Marine Geology*, 96(1–2), 175–185. [https://doi.org/10.1016/0025-3227\(91\)90215-p](https://doi.org/10.1016/0025-3227(91)90215-p)
- Herzberg, C., & Gazel, E. (2009). Petrological evidence for secular cooling in mantle plumes. *Nature*, 458(7238), 619–622. <https://doi.org/10.1038/nature07857>
- Hirano, N., Takahashi, E., Yamamoto, J., Abe, N., Ingle, S. P., Kaneoka, I., et al. (2006). Volcanism in Response to Plate Flexure. *Science*, 313(5792), 1426–1428. <https://doi.org/10.1126/science.1128235>
- Hirose, K., & Kushiro, I. (1993). Partial melting of dry peridotites at high pressures: Determination of compositions of melts segregated from peridotite using aggregates of diamond. *Earth and Planetary Science Letters*, 114(4), 477–489. [https://doi.org/10.1016/0012-821X\(93\)90077-M](https://doi.org/10.1016/0012-821X(93)90077-M)
- Hirschmann, M. M., Kogiso, T., Baker, M. B., & Stolper, E. M. (2003). Alkaline magmas generated by partial melting of garnet pyroxenite. *Geology*, 31(6), 481–484. [https://doi.org/10.1130/0091-7613\(2003\)031<0481:AMGBPM>2.0.CO;2](https://doi.org/10.1130/0091-7613(2003)031<0481:AMGBPM>2.0.CO;2)
- Hofmann, A. W., & White, W. M. (1982). Mantle plumes from ancient oceanic crust. *Earth and Planetary Science Letters*, 57(2), 421–436. [https://doi.org/10.1016/0012-821X\(82\)90161-3](https://doi.org/10.1016/0012-821X(82)90161-3)
- Holm, P. M. (1988). Nd, Sr, and Pb isotope geochemistry of the Lower Lavas, E Greenland Tertiary Igneous Province. *Geological Society, London, Special Publications*, 39(1), 181–195. <https://doi.org/10.1144/GSL.SP.1988.039.01.17>
- Ionov, D. A., Mukasa, S. B., & Bodinier, J.-L. (2002). Sr–Nd–Pb Isotopic Compositions of Peridotite Xenoliths from Spitsbergen: Numerical Modelling Indicates Sr–Nd Decoupling in the Mantle by Melt Percolation Metasomatism. *Journal of Petrology*, 43(12), 2261–2278. <https://doi.org/10.1093/petrology/43.12.2261>
- Irvine, T. N., & Baragar, W. R. A. (1971). A Guide to the Chemical Classification of the Common Volcanic Rocks. *Canadian Journal of Earth Sciences*, 8(5), 523–548. <https://doi.org/10.1139/e71-055>
- Jensen, S. M. (1998). Tertiary mineralization and magmatism, East Greenland: Lead isotope evidence for remobilization of continental crust. *Chemical Geology*, 150(1), 119–144. [https://doi.org/10.1016/S0009-2541\(98\)00063-1](https://doi.org/10.1016/S0009-2541(98)00063-1)
- Jones, R. E., van Keken, P. E., Hauri, E. H., Tucker, J. M., Vervoort, J., & Ballentine, C. J. (2019). Origins of the terrestrial Hf–Nd mantle array: Evidence from a combined geodynamical-geochemical approach. *Earth and Planetary Science Letters*, 518, 26–39. <https://doi.org/10.1016/j.epsl.2019.04.015>
- Kempton, P. D., Fitton, J. G., Saunders, A. D., Nowell, G. M., Taylor, R. N., Hardarson, B. S., & Pearson, G. (2000). The Iceland plume in space and time: A Sr–Nd–Pb–Hf study of the North Atlantic rifted margin. *Earth and Planetary Science Letters*, 177(3), 255–271. [https://doi.org/10.1016/S0012-821X\(00\)00047-9](https://doi.org/10.1016/S0012-821X(00)00047-9)
- Kharin, G. S., & Eroshenko, D. V. (2014). Magmatism: The Jan Mayen hotspot, Arctic Atlantic Ocean. *Journal of Volcanology and Seismology*, 8(2), 108–124. <https://doi.org/10.1134/S074204631402002X>
- Kincaid, C., Ito, G., & Gable, C. (1995). Laboratory investigation of the interaction of off-axis mantle plumes and spreading centres. *Nature*, 376(6543), 758–761. <https://doi.org/10.1038/376758a0>

- Kokfelt, T. F., Hoernle, K., Fiebig, J., Werner, R., & Garbe-Schönberg, D. (2006). Combined Trace Element and Pb-Nd-Sr-O Isotope Evidence for Recycled Oceanic Crust (Upper and Lower) in the Iceland Mantle Plume. *Journal of Petrology*, 47(9), 1705–1749. <https://doi.org/10.1093/ptrology/eg1025>
- Kokfelt, T. F., Hoernle, K., Lundstrom, C., Hauff, F., & van den Bogaard, C. (2009). Time-scales for magmatic differentiation at the Snaefellsjökull central volcano, western Iceland: Constraints from U–Th–Pa–Ra disequilibria in post-glacial lavas. *Geochimica et Cosmochimica Acta*, 73(4), 1120–1144. <https://doi.org/10.1016/j.gca.2008.11.021>
- Le Maitre, R. W., Streckeisen, A., Zanettin, B., Le Bas, M. J., Bonin, B., & Bateman, P. (Eds.) (2002). *Igneous rocks: A classification and glossary of terms* (2nd ed.). Cambridge University Press. <https://doi.org/10.1017/CBO9780511535581>
- Luais, B., & Hawkesworth, C. J. (2002). Pb isotope variations in Archaean time and possible links to the sources of certain Mesozoic–Recent basalts. *Geological Society, London, Special Publications*, 199(1), 105–124. <https://doi.org/10.1144/gsl.sp.2002.199.01.06>
- Manning, C. J., & Thirlwall, M. F. (2014). Isotopic evidence for interaction between Örefajökull mantle and the Eastern Rift Zone, Iceland. *Contributions to Mineralogy and Petrology*, 167(1), 959. <https://doi.org/10.1007/s00410-013-0959-1>
- Marquart, G., Schmeling, H., & Čadež, O. (2007). Dynamic models for mantle flow and seismic anisotropy in the North Atlantic region and comparison with observations. *Geochemistry, Geophysics, Geosystems*, 8(2), 39. <https://doi.org/10.1029/2006GC001359>
- McDonough, W. F., & Sun, S. (1995). The composition of the Earth. *Chemical Geology*, 120(3), 223–253. [https://doi.org/10.1016/0009-2541\(94\)00140-4](https://doi.org/10.1016/0009-2541(94)00140-4)
- McKenzie, D., & O’Nions, R. K. (1991). Partial Melt Distributions from Inversion of Rare Earth Element Concentrations. *Journal of Petrology*, 32(5), 1021–1091. <https://doi.org/10.1093/ptrology/32.5.1021>
- Melluso, L., Sethna, S. F., & Srivastava, R. (2021). First occurrence of melilite, potassic richterite, and tetraferriphlogopite in Deccan Trap-related alkaline rocks, and its petrogenetic significance: The Rajpuri ijolitenephelinite intrusion, Murud, Mumbai area, India. *J. Min. Geochem. 1971(1)*, 49–64. <https://doi.org/10.1127/njma/2020/0236>
- Melluso, L., Tucker, R. D., Cucciniello, C., le Roex, A. P., Morra, V., Zanetti, A., & Rakotoson, R. L. (2018). The magmatic evolution and genesis of the Quaternary basanite-trachyphonolite suite of Itasy (Madagascar) as inferred by geochemistry, Sr-Nd-Pb isotopes, and trace element distribution in coexisting phases. *Lithos*, 310–311, 50–64. <https://doi.org/10.1016/j.lithos.2018.04.003>
- Mertz, D. F., & Haase, K. M. (1997). The radiogenic isotope composition of the high-latitude North Atlantic mantle. *Geology*, 25(5), 411–414. [https://doi.org/10.1130/0091-7613\(1997\)025<0411:tricot>2.3.co;2](https://doi.org/10.1130/0091-7613(1997)025<0411:tricot>2.3.co;2)
- Mertz, D. F., & Renne, P. R. (1995). Quaternary multi-stage alkaline volcanism at Vesteris Seamount (Norwegian—Greenland Sea): Evidence from laser step heating ⁴⁰Ar/³⁹Ar experiments. *Journal of Geodynamics*, 19(1), 79–95. [https://doi.org/10.1016/0264-3707\(94\)e0001-b](https://doi.org/10.1016/0264-3707(94)e0001-b)
- Meyzen, C. M., Blichert-Toft, J., Ludden, J. N., Humler, E., Mével, C., & Albarède, F. (2007). Isotopic portrayal of the Earth’s upper mantle flow field. *Nature*, 447(7148), 1069–1074. <https://doi.org/10.1038/nature05920>
- Moreno, K. A., Thal, J., Bach, W., Beier, C., & Haase, K. M. (2021). Volcanic Structures and Magmatic Evolution of the Vesteris Seamount, Greenland Basin. *Frontiers in Earth Science*, 9, 711910. <https://doi.org/10.3389/feart.2021.711910>
- Morgan, W. J. (1972). Deep mantle convection plumes and plate motions. *AAPG Bulletin*, 56(2), 203–213. <https://doi.org/10.1306/819A3E50-16C5-11D7-8645000102C1865D>
- Müller, D., Seton, M., Zahirovic, S., Williams, S., Matthews, K., Wright, N., et al. (2016). Ocean basin evolution and global-scale plate reorganization events since Pangea breakup. *Annual Review of Earth and Planetary Sciences*, 44(1), 107–138. <https://doi.org/10.1146/annurev-earth-060115-012211>
- Negredo, A. M., van Hunen, J., Rodríguez-González, J., & Fullea, J. (2022). On the origin of the Canary Islands: Insights from mantle convection modelling. *Earth and Planetary Science Letters*, 584, 117506. <https://doi.org/10.1016/j.epsl.2022.117506>
- O’Connor, J. M., Stoffers, P., Wijbrans, J. R., Shannon, P. M., & Morrissey, T. (2000). Evidence from episodic seamount volcanism for pulsing of the Iceland plume in the past 70 Myr. *Nature*, 408(6815), 954–958. <https://doi.org/10.1038/35050066>
- Peate, D. W., Breddam, K., Baker, J. A., Kurz, M. D., Barker, A. K., Prestvik, T., et al. (2010). Compositional Characteristics and Spatial Distribution of Enriched Icelandic Mantle Components. *Journal of Petrology*, 51(7), 1447–1475. <https://doi.org/10.1093/ptrology/egq025>
- Pilidou, S., Priestley, K., Debayle, E., & Gudmundsson, Ó. (2005). Rayleigh wave tomography in the North Atlantic: High resolution images of the Iceland, Azores and Eifel mantle plumes. *Lithos*, 79(3), 453–474. <https://doi.org/10.1016/j.lithos.2004.09.012>
- Plank, T. (2014). The chemical composition of subducting sediments. In R. F. Keeling (Ed.), *Treatise on geochemistry* (pp. 607–629). Elsevier. <https://doi.org/10.1016/B978-0-08-095975-7.00319-3>
- Plank, T., & Langmuir, C. H. (1998). The chemical composition of subducting sediment and its consequences for the crust and mantle. *Chemical Geology*, 145(3), 325–394. [https://doi.org/10.1016/S0009-2541\(97\)00150-2](https://doi.org/10.1016/S0009-2541(97)00150-2)
- Prestvik, T., Goldberg, S., Karlsson, H., & Grönvold, K. (2001). Anomalous strontium and lead isotope signatures in the off-ridge Örefajökull central volcano in south-east Iceland: Evidence for enriched endmember(s) of the Iceland mantle plume? *Earth and Planetary Science Letters*, 190(3), 211–220. [https://doi.org/10.1016/S0012-821X\(01\)00390-9](https://doi.org/10.1016/S0012-821X(01)00390-9)
- Rankenburger, K., Lassiter, J. C., & Brey, G. (2005). The role of continental crust and lithospheric mantle in the genesis of Cameroon volcanic line lavas: Constraints from isotopic variations in lavas and megacrysts from the Biu and Jos Plateaux. *Journal of Petrology*, 46(1), 169–190. <https://doi.org/10.1093/ptrology/egh067>
- Révilion, S., Teagle, D. A. H., Boulvais, P., Shafer, J., & Neal, C. R. (2007). Geochemical fluxes related to alteration of a subaerially exposed seamount: Nintoku seamount, ODP Leg 197, Site 1205. *Geochemistry, Geophysics, Geosystems*, 8(2), Q02014. <https://doi.org/10.1029/2006GC001400>
- Ribe, N. M., & Christensen, U. R. (1999). The dynamical origin of Hawaiian volcanism. *Earth and Planetary Science Letters*, 171(4), 517–531. [https://doi.org/10.1016/S0012-821X\(99\)00179-X](https://doi.org/10.1016/S0012-821X(99)00179-X)
- Rickers, F., Fichtner, A., & Trampert, J. (2013). The Iceland–Jan Mayen plume system and its impact on mantle dynamics in the North Atlantic region: Evidence from full-waveform inversion. *Earth and Planetary Science Letters*, 367, 39–51. <https://doi.org/10.1016/j.epsl.2013.02.022>
- Ritsema, J., Deuss, A., van Heijst, H. J., & Woodhouse, J. H. (2011). S40RTS: A degree-40 shear-velocity model for the mantle from new Rayleigh wave dispersion, teleseismic traveltime and normal-mode splitting function measurements. *Geophysical Journal International*, 184(3), 1223–1236. <https://doi.org/10.1111/j.1365-246X.2010.04884.x>
- Rudnick, R. L., & Fountain, D. M. (1995). Nature and composition of the continental crust: A lower crustal perspective. *Reviews of Geophysics*, 33(3), 267–309. <https://doi.org/10.1029/95RG01302>
- Sandwell, D., & Fialko, Y. (2004). Warping and cracking of the Pacific plate by thermal contraction. *Journal of Geophysical Research*, 109(B10), B10411. <https://doi.org/10.1029/2004JB003091>
- Saunders, A. D., Fitton, J. G., Kerr, A. C., Norry, M. J., & Kent, R. W. (1997). The North Atlantic igneous province. In J. J. Mahoney, F. Millard, & M. F. Coffin (Eds.), *Large igneous provinces: Continental, oceanic and planetary flood volcanism* (pp. 45–93). American Geophysical Union Geophysical Monograph 100. Retrieved from <https://books.google.no/books?hl=en&lr=&id=5H8vobp2x3AC&oi=fnd&pg=PA1&dq>

- Sayyed, M. R. G. (2014). Lithological control on the mobility of elements during chemical weathering. *Comunicações Geológicas*, 101(1), 63–69.
- Schaeffer, A. J., & Lebedev, S. (2013). Global shear speed structure of the upper mantle and transition zone. *Geophysical Journal International*, 194(1), 417–449. <https://doi.org/10.1093/gji/ggt095>
- Schiffers, C., Balling, N., Ebbing, J., Jacobsen, B. H., & Nielsen, S. B. (2016). Geophysical-petrological modelling of the East Greenland Caledonides—Isostatic support from crust and upper mantle. *Tectonophysics*, 692, 44–57. <https://doi.org/10.1016/j.tecto.2016.06.023>
- Schiffers, C., Balling, N., Jacobsen, B. H., Stephenson, R. A., & Nielsen, S. B. (2014). Seismological evidence for a fossil subduction zone in the East Greenland Caledonides. *Geology*, 42(4), 311–314. <https://doi.org/10.1130/G35244.1>
- Schiffers, C., Doré, A. G., Foulger, G. R., Franke, D., Geoffroy, L., Gernigon, L., et al. (2020). Structural inheritance in the North Atlantic. *Earth-Science Reviews*, 206, 102975. <https://doi.org/10.1016/j.earscirev.2019.102975>
- Schilling, J.-G., Kingsley, R., Fontignie, D., Poreda, R., & Xue, S. (1999). Dispersion of the Jan Mayen and Iceland mantle plumes in the Arctic: A He-Pb-Nd-Sr isotope tracer study of basalts from the Kolbeinsey, Mohns, and Knipovich Ridges. *Journal of Geophysical Research*, 104I(B5), 10543–10570. <https://doi.org/10.1029/1999JB900057>
- Schilling, J.-G., & Noe-Nygaard, A. (1974). Faeroe-Iceland plume: Rare-earth evidence. *Earth and Planetary Science Letters*, 24(1), 1–14. [https://doi.org/10.1016/0012-821X\(74\)90002-8](https://doi.org/10.1016/0012-821X(74)90002-8)
- Schmidt, R. A. L. F., Schmincke, H. U., Sigurdsson, H., Houghton, B., McNutt, S., Rymer, H., & Stix, J. (2000). Seamounts and island building. In *Encyclopedia of volcanoes* (pp. 383–402).
- Simmons, N. A., Forte, A. M., Boschi, L., & Grand, S. P. (2010). GyPSuM: A joint tomographic model of mantle density and seismic wave speeds. *Journal of Geophysical Research*, 115(B12). <https://doi.org/10.1029/2010JB007631>
- Sobolev, A., Hofmann, A., & Nikogosian, I. (2000). Recycled oceanic crust observed in 'ghost plagioclase' within the source of Mauna Loa lavas. *Nature*, 404(6781), 986–990. <https://doi.org/10.1038/35010098>
- Stacey, J. S., & Kramers, J. D. (1975). Approximation of terrestrial lead isotope evolution by a two-stage model. *Earth and Planetary Science Letters*, 26(2), 207–221. [https://doi.org/10.1016/0012-821X\(75\)90088-6](https://doi.org/10.1016/0012-821X(75)90088-6)
- Starkey, N. A., Stuart, F. M., Ellam, R. M., Fitton, J. G., Basu, S., & Larsen, L. M. (2009). Helium isotopes in early Iceland plume picrites: Constraints on the composition of high ³He/⁴He mantle. *Earth and Planetary Science Letters*, 277(1–2), 91–100. <https://doi.org/10.1016/j.epsl.2008.10.007>
- Staudigel, H., Plank, T., White, B., & Schmincke, H.-U. (1996). Geochemical fluxes during seafloor alteration of the basaltic upper oceanic crust: DSDP sites 417 and 418. In *Washington DC American geophysical union geophysical monograph series* (Vol. 96, pp. 19–38). <https://doi.org/10.1029/GM096p0019>
- Stecher, O., Carlson, R. W., & Gunnarsson, B. (1999). Torfajökull: A radiogenic end-member of the Iceland Pb-isotopic array. *Earth and Planetary Science Letters*, 165(1), 117–127. [https://doi.org/10.1016/S0012-821X\(98\)00256-8](https://doi.org/10.1016/S0012-821X(98)00256-8)
- Steinberger, B., & Becker, T. W. (2018). A comparison of lithospheric thickness models. *Tectonophysics*, 746, 325–338. <https://doi.org/10.1016/j.tecto.2016.08.001>
- Storey, M., Pedersen, A. K., Stecher, O., Bernstein, S., Larsen, H., Larsen, L., et al. (2004). Long-lived postbreakup magmatism along the East Greenland margin: Evidence for shallow-mantle metasomatism by the Iceland plume. *Geology*, 32(2), 173–179. <https://doi.org/10.1130/g19889.1>
- Stracke, A. (2012). Earth's heterogeneous mantle: A product of convection-driven interaction between crust and mantle. *Chemical Geology*, 330–331, 274–299. <https://doi.org/10.1016/j.chemgeo.2012.08.007>
- Sun, S., & McDonough, W. F. (1989). Chemical and isotopic systematics of oceanic basalts: Implications for mantle composition and processes. *Geological Society, London, Special Publications*, 42(1), 313–345. <https://doi.org/10.1144/GSL.SP.1989.042.01.19>
- Talwani, M., & Eldholm, O. (1977). Evolution of the Norwegian-Greenland Sea. *GSA Bulletin*, 88(7), 969–999. [https://doi.org/10.1130/0016-7606\(1977\)88<969:Eotms>2.0.Co;2](https://doi.org/10.1130/0016-7606(1977)88<969:Eotms>2.0.Co;2)
- Thirlwall, M. F., Gee, M. A. M., Taylor, R. N., & Murton, B. J. (2004). Mantle components in Iceland and adjacent ridges investigated using double-spike Pb isotope ratios. *Geochimica et Cosmochimica Acta*, 68(2), 361–386. [https://doi.org/10.1016/S0016-7037\(03\)00424-1](https://doi.org/10.1016/S0016-7037(03)00424-1)
- Thirlwall, M. F., Upton, B. G. J., & Jenkins, C. (1994). Interaction between Continental Lithosphere and the Iceland Plume—Sr-Nd-Pb Isotope Geochemistry of Tertiary Basalts, NE Greenland. *Journal of Petrology*, 35(3), 839–879. <https://doi.org/10.1093/ptrology/35.3.839>
- Thompson, R. N., & Gibson, S. A. (1991). Subcontinental mantle plumes, hotspots and pre-existing thinspots. *Journal of the Geological Society*, 148(6), 973–977. <https://doi.org/10.1144/gsjgs.148.6.0973>
- Torsvik, T. H., Amundsen, H. E. F., Trønnes, R. G., Doubrovine, P. V., Gaina, C., Kuznir, N. J., et al. (2015). Continental crust beneath southeast Iceland. *Proceedings of the National Academy of Sciences*, 112(15), E1818–E1827. <https://doi.org/10.1073/pnas.1423099112>
- Toyokuni, G., Matsuno, T., & Zhao, D. (2020). P wave tomography beneath Greenland and surrounding regions: I. Crust and upper mantle. *Journal of Geophysical Research: Solid Earth*, 125(12), e2020JB019837. <https://doi.org/10.1029/2020JB019837>
- Trønnes, R. G., Planke, S., Sundvoll, B., & Imsland, P. (1999). Recent volcanic rocks from Jan Mayen: Low-degree melt fractions of enriched northeast Atlantic mantle. *Journal of Geophysical Research*, 104(B4), 7153–7168. <https://doi.org/10.1029/1999jb900007>
- Vervoort, J. D., & Blichert-Toft, J. (1999). Evolution of the depleted mantle: Hf isotope evidence from juvenile rocks through time. *Geochimica et Cosmochimica Acta*, 63(3), 533–556. [https://doi.org/10.1016/S0016-7037\(98\)00274-9](https://doi.org/10.1016/S0016-7037(98)00274-9)
- Vervoort, J. D., Plank, T., & Prytulak, J. (2011). The Hf-Nd isotopic composition of marine sediments. *Geochimica et Cosmochimica Acta*, 75(20), 5903–5926. <https://doi.org/10.1016/j.gca.2011.07.046>
- Vogt, P. R., Kovacs, L. C., Bernero, C., & Srivastava, S. P. (1982). Asymmetric geophysical signatures in the Greenland-Norwegian and Southern Labrador Seas and the Eurasia Basin. *Tectonophysics*, 89(1), 95–160. [https://doi.org/10.1016/0040-1951\(82\)90036-1](https://doi.org/10.1016/0040-1951(82)90036-1)
- Vogt, P. R., & Smoot, N. C. (1984). The Geisha Guyots: Multibeam bathymetry and morphometric interpretation. *Journal of Geophysical Research*, 89(B13), 11085–11107. <https://doi.org/10.1029/JB089iB13p11085>
- Voss, M., Schmidt-Aursch, M. C., & Jokat, W. (2009). Variations in magmatic processes along the East Greenland volcanic margin. *Geophysical Journal International*, 177(2), 755–782. <https://doi.org/10.1111/j.1365-246X.2009.04077.x>
- Wang, T., Lin, J., Tucholke, B., & Chen, Y. J. (2011). Crustal thickness anomalies in the North Atlantic Ocean basin from gravity analysis. *Geochemistry, Geophysics, Geosystems*, 12(3), Q0AE02. <https://doi.org/10.1029/2010GC003402>
- Weis, D., Kieffer, B., Hanano, D., Nobre Silva, I., Barling, J., Pretorius, W., et al. (2007). Hf isotope compositions of U.S. Geological Survey reference materials. *Geochemistry, Geophysics, Geosystems*, 8(6), Q06006. <https://doi.org/10.1029/2006GC001473>
- Weis, D., Kieffer, B., Maerschalk, C., Barling, J., de Jong, J., Williams, G. A., et al. (2006). High-precision isotopic characterization of USGS reference materials by TIMS and MC-ICP-MS. *Geochemistry, Geophysics, Geosystems*, 7(8), Q08006. <https://doi.org/10.1029/2006GC001283>
- Wessel, P., Sandwell, D. T., & Kim, S.-S. (2010). The global seamount census. *Oceanography*, 23(1), 24–33. <https://doi.org/10.5670/oceanog.2010.60>

- White, S. M. (2005). Seamounts. In R. C. Selley, L. R. M. Cocks, & I. R. Plimer (Eds.), *Encyclopedia of geology* (pp. 475–484). Elsevier. <https://doi.org/10.1016/B0-12-369396-9/00450-0>
- Willbold, M., & Stracke, A. (2006). Trace element composition of mantle end-members: Implications for recycling of oceanic and upper and lower continental crust. *Geochemistry, Geophysics, Geosystems*, 7(4), 1–30. <https://doi.org/10.1029/2005GC001005>
- Wilson, J. T. (1963). A possible origin of the Hawaiian Islands. *Canadian Journal of Physics*, 41(6), 863–870. <https://doi.org/10.1139/p63-094>
- Workman, R. K., & Hart, S. R. (2005). Major and trace element composition of the depleted MORB mantle (DMM). *Earth and Planetary Science Letters*, 231(1), 53–72. <https://doi.org/10.1016/j.epsl.2004.12.005>
- Yaxley, G. M., & Green, D. H. (1998). Reactions between eclogite and peridotite: Mantle refertilisation by subduction of oceanic crust. *Schweizerische mineralogische und petrographische Mitteilungen*, 78(2), 243–255.
- Zartman, R. E., & Doe, B. R. (1981). Plumbotectonics—The model. *Tectonophysics*, 75(1), 135–162. [https://doi.org/10.1016/0040-1951\(81\)90213-4](https://doi.org/10.1016/0040-1951(81)90213-4)
- Zartman, R. E., & Haines, S. M. (1988). The plumbotectonic model for Pb isotopic systematics among major terrestrial reservoirs—A case for bi-directional transport. *Geochimica et Cosmochimica Acta*, 52(6), 1327–1339. [https://doi.org/10.1016/0016-7037\(88\)90204-9](https://doi.org/10.1016/0016-7037(88)90204-9)
- Zhang, T., Lin, J., & Gao, J. (2020). Asymmetric crustal structure of the ultraslow-spreading Mohs Ridge. *International Geology Review*, 62(5), 568–584. <https://doi.org/10.1080/00206814.2019.1627586>